UNIVERSITY OF CALIFORNIA SAN DIEGO

Flexible and Wearable Silver/Silver Chloride Multi-Electrode Array for Active Monitoring of Various Human Electrical Signals

A dissertation submitted in partial satisfaction of the
requirements for the degree Doctor of Philosophy

in

Materials Science and Engineering

by

Jonas F. Kurniawan

Committee in Charge:

Professor Todd P. Coleman, Chair
Professor Shadi A. Dayeh
Professor Darren J. Lipomi
Professor Tse Nga (Tina) Ng
Professor Sheng Xu

2021

The Dissertation of Jonas F. Kurniawan is approved, and it is acceptable in quality and form for publication on microfilm and electronically.

University of California San Diego
2021

DEDICATION

To my parents, family, and friends.

EPIGRAPH

I am the master of my fate: I am the captain of my soul.

Invictus
William E. Henley

TABLE OF CONTENTS

LIST OF FIGURES

LIST OF TABLES

ACKNOWLEDGEMENTS

Firstly, I would like to thank my doctoral advisor, Professor Todd P. Coleman. Todd has played a critical role in my development as a researcher and inventor. His mentorship, both by direct discussion and feedback has changed the way I approach research and think about challenging problems. His constant support, wit, humor, life lessons, and pragmatic attitude have simply made my PhD work much more enjoyable.

Next, I would like to thank Professor John A. Rogers and Professor Brian T. Cunningham whom I met at University of Illinois at Urbana-Champaign during my formative years as an undergraduate researcher. They provided me with several years of valuable research mentorship. They inspired me to pursue graduate research in my quest to solve problems and deepen my understanding of the scientific world.

I would like to also thank my undergraduate advisor and professors, Professor Angus Rockett and Professor Leslie Allen. Angus has played a pivotal role in my undergraduate education. He was always there to advise me and guided me to the right direction whenever I faced roadblocks. He always pushed me to be a better version of myself. Meanwhile, Les got me interested in electronics materials after taking his class. His approach really changed my perspective for learning. I will always remember the two summers we had in Blackeet Indian Reservation, Montana, where we led NSF scientific outreach workshops for middle and high school students. It was a genuinely satisfying experience witnessing how these students were so inspired to be future scientists and engineers after attending our workshops. I am always grateful for this experience as it taught me a valuable lesson that I could always make an impact in this world with my knowledge/expertise.

I would like to thank my undergraduate research mentors, namely R. Chad Webb, Siddharth Krishnan, and Weili Chen. They played an important role in molding my research skills over my formative years at UIUC. They taught me to never give up on challenging problems and be systematic when solving them. They have ingrained tenacity and perseverance in me. Their wonderful mentorship inspired me pass the skills and knowledge in a similar manner to all the mentees that I had the opportunities to work with throughout my graduate study.

My graduate research would not have been possible without the assistance of my wonderful undergraduate mentees whom I had the pleasure working with for over four productive years. I have been very fortunate to have mentored seven outstanding students, namely Andrew J. Shin, Boris Tjhia, Minyul (Mike) Lee, Carleen Li, Nathan L. J. Sit, Timothy Pham, and last but not least Andrew K. L. Nguyen. They have my gratitude for their hard work and camaraderie over my time at UCSD. It is my hope that they learnt as much from me as I did from them.

I would also like to thank the members of Neural Interaction Laboratory (NIL) who provided me with assistance and support throughout my graduate study. Special thanks to Dr. Phillip Kyriakakis whom I always enjoy talking to about various topics whenever I am in the lab. Further, I thank Dr. Rajan Kumar, Dr. Alexis Allegra, Dr. Gladys Ornelas, and Vincent M. Wu for all the knowledge you all shared with me and for our successful collaborations.

Further, I would like to thank my numerous external collaborators, including but not limited to Professor Imanuel Lerman, MD, Yifeng Bu, and Brandon Ho at the Department of Anesthesiology/Department of Electrical and Computer Engineering, UC San Diego; Professor David Kunkel, MD at the Department of Medicine, UC San Diego; Professor Yahir Santiago-Lastra and Dr. Sanghee Lee at the Department of Urology, UC San Diego. My work would not have been possible without them.

I would like to thank my doctoral committee members Professors Shadi A. Dayeh, Darren J. Lipomi, Tse Nga (Tina) Ng, and Sheng Xu. I have had the opportunity to learn from them in many settings such as collaborations, lectures, discussions, and feedback providers, over the past five years. They bring unique insights to my work and taught me how to be successful in my doctoral research.

My gratitude extends to all the previous and existing staff in Nano3 who have supported me and my undergraduate mentees throughout my graduate study with meaningful discussions and assistance. Special thanks to Dr. Bernd Fruhberger for your guidance; Larry Grissom who taught me about best practices in lithography; Sean Parks, Ahdam Ali, Hal Romans for best practices in deposition; Patrick Driscoll and Ivan Harris for best practices in dry etching; Ryan Anderson and Dr. Ryan Nicholl for teaching me about SEM; Dr. John Tamelier, Dr. Xuekun Lu, and Shu Xiang for our discussions about microfabrication processing; last but not least David Prescott whom I always enjoy chatting with about processes whenever I am in the cleanroom, and when outside enjoy playing a round of golf with.

I would like to thank my academic advisors in the Materials Science and Engineering Program, Katie Hamilton and Akemi Alpaslan. Katie convinced me to join Materials Science and Engineering at UC San Diego over our initial phone call back in 2016 when I first got admitted to the program; without her, I would not have been here today. Katie and Akemi have also played crucial supporting roles in helping me navigate the MATS PhD program with such ease.

Thanks also go out to staff in the Bioengineering Department, namely Douglas Gurevitch, Katia Vallejo, Omar Vazquez, and Janice Leung. They were always there to assist me in many things including but not limited to receiving packages, lab safety, purchasing, funding, and so on. Their support has been crucial during my time at the department.

To my friends from the UCSD Badminton Club and APD Consulting Club, thank you. They have been the most wonderful, fun, and understanding group of friends I could ever ask for. They have been my constant sources of happiness throughout the years whenever I need to unwind from the lab.

I would like to thank my friends whom I met through the IGE Program back in 2017, Gopesh Tilvawala and Jordan Furlong. Gopesh has always been there for me through thick and thin. I am grateful for his friendship, invaluable advice, and support that he has given me throughout the years. He has also introduced me to Gujarati cuisine, it is very unique and before that I have never known that vegetables can taste that good. Jordan is always fun to hangout with and down to play a round of golf with me. I am grateful for their friendship throughout my time at UCSD.

I am also thankful to Dean Steve Cassedy whom I met during my first year in graduate school. Dean Cassedy has played a pivotal role in supporting me throughout my graduate study. He shared his wisdom and advice whenever I faced problems, I am always grateful to have had his mentorship and support.

My success would not have been possible without the love and support of my family. To my parents, Adi Kurniawan and Nanik R. Tantoro, for patiently bringing me up and always provided me with opportunities to succeed. As a boy, they always encouraged my curious self to learn about how the world works which motivated me to a problem solver. Although, I have left home since I was 15 to study abroad, they were always there for me. They ingrained in me the value of hard work and ethics by never allowing me to be complacent and making sure I am doing what is right. To my brother and sister, Joshua Timoti and Joan Tessalonika, thank you for all the fun and laughter we had growing up. Playing badminton, soccer, and basketball in our yard will

always be memories I cherish the most. Tessa is always one phone call away whenever I need help or advice. Joshua, on the other hand is halfway across the world. I know I can always rely on you about any medical advice. Let's have fun like the good old days when I visit back home!

Lastly, I would like to thank my partner, Jelita C. Pertiwi, who I met in college back when I was a junior. We supported each other as we both worked towards our goals. Although distance separated us for the past five years, we somehow managed to build an amazing relationship while at the same time dealing with the struggles and stresses of graduate school/job and the often failed experiments. I could not have done it without your support. Having finished her Master's degree, she has spent the past three years working as a crop scientist. She always encourages me whenever I am discouraged, cheers me up whenever I feel down, and most importantly understanding that completing my graduate degree requires sacrifices from both of us. As we move on to our next steps together, I hope to support her as she has supported me.

Chapter 1, in full, is a reprint of the material as it appears in Advanced Materials Technologies, 2020. Jonas F. Kurniawan, Boris Tjhia, Vincent M. Wu, Andrew Shin, Nathan L. J. Sit, Timothy Pham, Andrew Nguyen, Carleen Li, Rajan Kumar, Marcelo Aguilar-Rivera, Imanuel Lerman, David C. Kunkel, Todd P. Coleman. The dissertation author was the primary investigator of this material.

Chapter 2, in full, is currently being prepared for submission for publication of this material. Jonas F. Kurniawan, Alexis Allegra, Timothy Pham, Andrew K. L. Nguyen, Nathan L. J. Sit, Boris Tjhia, Andrew J. Shin, Todd P. Coleman. The dissertation author was the primary investigator of this material.

Chapter 3 in full, is currently being prepared for submission for publication of this material. Yifeng Bu, Jonas F. Kurniawan, Andrew K. L. Nguyen, Brandon Ho, Nathan L. J. Sit, Timothy

Pham, Vincent M. Wu, Boris Tjhia, Andrew J. Shin, Todd P. Coleman, Imanuel Lerman. The dissertation author was the primary investigator of this material.

Chapter 4 in full, is currently being prepared for submission for publication of this material. Jonas F. Kurniawan, Sanghee Lee, Hoang-Kim Le, Andrew K. L. Nguyen, Nathan L.J. Sit, Timothy Pham, Boris Tjhia, Ryan Gottlieb, Carleen Li, Andrew J. Shin, Hassler Bueno Garcia, Vincent M. Wu, Tris R Mendoza, Thomas DiPina, George Chiang, Gladys Ornelas, Christina A.M. Jamieson, Yahir Santiago-Lastra, Todd P. Coleman. The dissertation author was the primary investigator of this material.

VITA

EDUCATION

2015 *Bachelor of Science*, Materials Science and Engineering, University of Illinois at Urbana-Champaign

2017 *Master of Science*, Materials Science and Engineering, University of California San Diego

2021 *Doctor of Philosophy*, Materials Science and Engineering, University of California San Diego

WORK EXPERIENCE

2012 Summer Research Intern, Universidad Pontificia Comillas, Madrid, Spain

2012 – 2015 Lead Undergraduate Research Assistant, Rogers Research Group, Department of Materials Science and Engineering, University of Illinois at Urbana-Champaign

2013 – 2015 Undergraduate Research Assistant, Nanosensors Group, Department of Electrical and Computer Engineering, University of Illinois at Urbana-Champaign

2014 – 2015 Cleanroom Assistant, Frederick Seitz Materials Research Laboratory, University of Illinois at Urbana-Champaign

2015 – 2016 Research Associate, WeariFi Inc., Champaign, IL

2015 – 2016 Product Manager, NeuroLux Inc., Champaign, IL

2015 – 2016 Visiting Scholar, Rogers Research Group, Department of Materials Science and Engineering, University of Illinois at Urbana-Champaign

2016 – 2021 Graduate Research Assistant, University of California San Diego

2021 Teaching Assistant, University of California San Diego

ACTIVITES

Illini Badminton Intercollegiate Sports Club (IBIS), University of Illinois at Urbana-Champaign
2011 – 2016 Player
2013 – 2015 President

Institute for the Global Entrepreneur (IGE), University of California San Diego
2017 – 2018 IGE Fellow

UC San Diego Badminton Club, University of California San Diego
2016 – 2021 Player
2016 – 2021 Mentor

Advanced Professional Degree Consulting Club (APDCC), University of California San Diego
2019 – 2021 Consultant and Project Leader
2019 – 2020 VP Organizational Development
2020 – 2021 Co-President

PUBLICATIONS

1. Webb, R. C., Pielak, R. M., Bastien, P., Ayers, J., Niittynen, J., **Kurniawan, J.**, ... & Balooch, G. (2015). Thermal transport characteristics of human skin measured in vivo using ultrathin conformal arrays of thermal sensors and actuators. *PloS One*, *10*(2), e0118131.

2. Webb, R. C., Ma, Y., Krishnan, S., Li, Y., Yoon, S., Guo, X., ... & **Kurniawan, J.** (2015). Epidermal devices for noninvasive, precise, and continuous mapping of macrovascular and microvascular blood flow. *Science Advances*, *1*(9), e1500701.

3. Chen, W., Long, K. D., **Kurniawan, J.**, Hung, M., Yu, H., Harley, B. A., & Cunningham, B. T. (2015). Planar Photonic Crystal Biosensor for Quantitative Label-Free Cell Attachment Microscopy. *Advanced Optical Materials*, *3*(11), 1623-1632.

4. Zhang, Y., Chad Webb, R., Luo, H., Xue, Y., **Kurniawan, J.**, Cho, N. H., ... & Rogers, J. A. (2016). Theoretical and experimental studies of epidermal heat flux sensors for measurements of core body temperature. *Advanced Healthcare Materials*, *5*(1), 119-127.

5. Bandodkar, A. J., You, J. M., Kim, N. H., Gu, Y., Kumar, R., Mohan, A. V., **Kurniawan, J.**, ... & Parthasarathy, M. (2017). Soft, stretchable, high power density electronic skin-based biofuel cells for scavenging energy from human sweat. *Energy & Environmental Science*, *10*(7), 1581-1589.

6. Shin, G., Gomez, A. M., Al-Hasani, R., Jeong, Y. R., Kim, J., Xie, Z., ... & **Kurniawan, J.** (2017). Flexible near-field wireless optoelectronics as subdermal implants for broad applications in optogenetics. *Neuron*, *93*(3), 509-521.

7. Mohan, A. V., Kim, N., Gu, Y., Bandodkar, A. J., You, J. M., Kumar, R., **Kurniawan, J.**, Xu, S. & Wang, J. (2017). Merging of Thin-and Thick-Film Fabrication Technologies: Toward Soft Stretchable "Island–Bridge" Devices. *Advanced Materials Technologies*, *2*(4), 1600284.

8. Krishnan, S., Shi, Y., Webb, R. C., Ma, Y., Bastien, P., Crawford, K. E., Wang, A., Feng, X., Manco, M., **Kurniawan, J.**, ... & Rogers, J. A. (2017). Multimodal epidermal devices for hydration monitoring. *Microsystems & Nanoengineering*, *3*(1), 1-11.

9. Tian, L., Li, Y., Webb, R. C., Krishnan, S., Bian, Z., Song, J., Ning, X., Crawford, K., **Kurniawan, J.**, ... & Ma, J. (2017). Flexible and stretchable 3ω sensors for thermal characterization of human skin. *Advanced Functional Materials*, *27*(26), 1701282.

10. Martín, A., Kim, J., **Kurniawan, J. F.**, Sempionatto, J. R., Moreto, J. R., Tang, G., ... & Wang, J. (2017). Epidermal microfluidic electrochemical detection system: Enhanced sweat sampling and metabolite detection. *ACS Sensors*, *2*(12), 1860-1868.

11. Yin, L., Seo, J. K., **Kurniawan, J.**, Kumar, R., Lv, J., Xie, L., ... & Wang, J. (2018). Highly Stable Battery Pack via Insulated, Reinforced, Buckling-Enabled Interconnect Array. *Small*, *14*(43), 1800938.

12. Soto, F., Jeerapan, I., Silva-López, C., Lopez-Ramirez, M. A., Chai, I., Xiaolong, L., Jian, L., **Kurniawan, J. F.**, ... & Wang, J. (2018). Noninvasive transdermal delivery system of lidocaine using an acoustic droplet-vaporization based wearable patch. *Small*, *14*(49), 1803266.

13. Sempionatto, J. R., Martin, A., García-Carmona, L., Barfidokht, A., **Kurniawan, J. F.**, Moreto, J. R., ... & Wang, J. (2019). Skin-worn Soft Microfluidic Potentiometric Detection System. *Electroanalysis*, *31*(2), 239-245.

14. **Kurniawan, J. F.**, Agrusa, A. S., Wu, V., Lerman, I. R., Kunkel, D. C., & Coleman, T. P. (2020). Su1356 STRETCHABLE ADHESIVE-INTEGRATED ELECTRONICS FOR MULTIELECTRODE CUTANEOUS GASTRIC SLOW WAVE MONITORING. *Gastroenterology*, *158*(6), S-563.

15. **Kurniawan, J. F.**, Tjhia, B., Wu, V. M., Shin, A., Sit, N. L., Pham, T., ... & Coleman, T. P. (2021). An Adhesive-Integrated Stretchable Silver-Silver Chloride Electrode Array for Unobtrusive Monitoring of Gastric Neuromuscular Activity. *Advanced Materials Technologies*, *6*(5), 2001229.

16. **Kurniawan, J. F.**, Lee, S., Le, H., Nguyen, A. K. L, Sit, N. L. J, Pham, T., Tjhia, B., Gottlieb, R., Li, C., Shin. A. J., Garcia, H. B., Wu, V. M., Mendoza, T. R., DiPina, T., Chiang, G., Ornelas, G., Jamieson, C. A. M, Santiago-Lastra, Y. & Coleman, T. P. (2021). "Non-Invasive Multi-Channel Urodynamic (NI Multi-Channel UDS) System is Sensitive and Reliable to Detect Inter-Subject Consistency of Electrical Signals from Human Urinary Bladder". *In Preparation*.

17. **Kurniawan, J. F.**, Allegra, A., Pham, T., Nguyen, A. K. L., Sit, N. L. J., Tjhia, B., Shin, A. J. & Coleman, T, P. (2021). "Electrochemical Performance Study of Ag/AgCl and Au Flexible Electrodes for Unobtrusive Monitoring of Human Biopotentials". *In Preparation*.

18. Bu, Y., **Kurniawan, J. F.**, Nguyen, A. K. L., Ho, B., Sit, N. L. J., Pham, T., Wu, V. M., Tjhia, B., Shin, A. J., Coleman, T.P. & Lerman, I. (2021). "Non-Invasive Measurement of Cervical Neuronal Activities via an Adhesive-Integrate Flexible Surface Electrodes". *In Preparation*.

19. Ornelas, G., **Kurniawan, J. F.**, Nguyen, A., Pham, T., Sit, N. L. J., Weissbrod, P. A. & Coleman T. P. (2021). "Flexible Electronic Sensors for Unobtrusive Monitoring of Laryngeal Electromyography". *In Preparation*.

20. Allegra, A. B., **Kurniawan, J. F.**, Kunkel, D. C., Pham, T., Nguyen, A. K. L., Sit, N. L. J., Tjhia, B., Shin, A. J. & Coleman, T. P. (2021). "Electrode Optimization for Bayesian Inference Based Gastric Slow Wave Source Localization". *In Preparation*.

FIELDS OF STUDY

Major Field: Materials Science and Engineering, Bioengineering, Flexible Electronics

Studies in Materials Science and Engineering

Professor Todd P. Coleman

ABSTRACT OF THE DISSERTATION

Flexible and Wearable Silver/Silver Chloride Multi-Electrode Array for Active Monitoring of Various Human Electrical Signals

by

Jonas F. Kurniawan
Doctor of Philosophy in Materials Science and Engineering
University of California San Diego, 2021
Professor Todd P. Coleman, Chair

Flexible and wearable electronics have become ubiquitous since the introduction of the first epidermal electronics back in 2011. Since then, many sensors various active materials have been developed to monitor various human electrical signals such as through electrocardiography (ECG), electrocorticography (ECoG), electroencephalography (EEG), and electromyography (EMG). These sensors usually typically are built in either thin (standard CMOS processes) or thick film technology (printing techniques). In thin film technology, gold and platinum often are chosen as the material of choice due to its ease in processing. Similarly, in thick film technology (printing), there is a larger selection of materials available, such as carbon black, carbon nanotube, and silver/silver chloride, to name a few.

While typical metals such as gold and platinum suffice for recording of most human electrical signals (higher frequency range), it is not ideal for the recording of the stomach electrical activity via electrogastrography (EGG), which is mostly at the low frequency region (~0.05 Hz). At low frequency (near DC), those metallic materials are polarizable in nature, thus very

susceptible to DC noise. Further, the high electrode-skin impedance due to low ion mobility will form a barrier for the biopotential waveform to cross. In this dissertation, I explore ways to marry techniques from thin and thick film technology, resulting in an adhesive-integrated flexible and wearable sensor array with very thin form factor and able to leverage Ag/AgCl as its active electrode's material.

In Chapter 1, I successfully explore this novel technique to yield an electrode array for the recording of electrogastrography (EGG) in healthy human subjects. The electrode array is successful in capturing the electrophysiological signal at the frequency domain associated with the stomach activity.

In Chapter 2, I conduct an electrochemical performance characterization study of the flexible electrode across multiple diameters, materials, and frequency ranges. The data are then fitted with a custom circuit model that describes the electrode/electrolyte behavior. This chapter will pave a foundation for future systematic design of electrode arrays by optimizing their properties for various biopotential recording applications.

In Chapter 3, I successfully explore the recording of cervical neuronal activities associated with parasympathetic and sympathetic nervous system using the custom flexible electrode array that attaches to the location on the neck where vagus nerve is approximately located under it. This work successfully presents a non-invasive neuronal recording technique that has not been explored in human subjects (previous work was only done on a rat model).

In Chapter 4, I successfully design a multi-electrode array that is capable of recording electromyography (EMG) activity from the human bladder muscles. This work hopefully will pioneer the breakthrough in non-invasive urodynamics studies to address the drawbacks of current urodynamics approaches. The drawbacks include invasive monitoring via an indwelling catheter,

discomfort or pain to the patient, a risk of urinary tract infection (UTI), and a risk of artifact due to filling of bladder at supra-physiologic rates.

While my approach of constructing flexible and wearable multi-electrode array has been successful in monitoring several human electrophysiological signals in healthy subjects, further validations through larger clinical trials are needed to prove adoption and clinical usefulness among larger patient population. Regardless, this body of work represents a critical step towards clinical non-invasive measures of human physiology.

Chapter 1. An Adhesive Integrated Stretchable Ag/AgCl Electrode Array for Unobtrusive Monitoring of Gastric Neuromuscular Activity

Abstract

Here, an unobtrusive, adhesive-integrated electrode array for continuous monitoring of stomach electric activity is introduced. This patient-friendly, disposable peel-and-stick adhesive device represents an important advancement over existing arrays that require placement of each electrode individually and are thus also labor intensive and are in general more rigid and cumbersome. In comparison to other silver–silver chloride electrodes, this skin conformal array does not require gel and thus can withstand low impedance over the duration of long recordings. Interfacing these electrodes with miniaturized electronic recording and wireless telemetry systems has the potential to enable scalable population health opportunities to perform objective gastrointestinal assessment and optimization of treatment regimens.

Keywords: digestive system, electrode array electrophysiology, gastrointestinal motility, neuromuscular activities, stretchable electronics, wearable monitoring.

Introduction

Gastrointestinal (GI) problems are the second leading cause of missing school or work after the common cold [1]. The financial burden associated with GI problems is estimated to be $142B annually [2]. A majority of such cases are referred to GI specialists, where endoscopy, imaging, and blood tests readily allow for easy diagnosis of structural and inflammatory pathology, such as a blockage or infection. However, more than half of GI disorders involve an abnormal functioning of the GI tract, in the absence of any structural defect, and these types of disorders occur in a majority of Parkinson's and diabetes patients for instance [3,4]. Diagnosis of such "functional" GI disorders typically entails subjective symptom-based questionnaires or objective but invasive procedures (e.g., gastric scintigraphy and manometry) in specialized centers. Symptom-based diagnosis is problematic because many GI functional disorders with different treatment regimens have overlapping symptoms. Most current clinically indicated objective approaches have drawbacks of cost and invasiveness. For instance, gastric involves radioactive imaging and manometry involves a catheter inserted through the mouth or nose with fluoroscopic or endoscopic guidance. With regards to disorders involving the foregut, motor aspects of stomach function do not correlate robustly with symptoms before or after treatment [5=7]. However, recent findings with invasive recordings show that electrical patterns of the stomach align well with dis- ease diagnosis, symptoms, as well as treatment response [8-12]. As such, there is a unique opportunity to extract this spatial electrical information non-invasively.

GI smooth muscle contractions are governed by underlying rhythmic bio–electrical signals, known as slow waves, that are generated by oscillating pacemaker cells, the interstitial cells of Cajal. These slow waves have a frequency of 0.05 Hz in the stomach and underlie the electrogastrogram (EGG) signal that can be recorded non-invasively with electrodes placed on the

abdomen [13].

Although it is non-invasive and easy to administer, conventional EGG suffers from limitations in interpretability and insufficient association with invasive clinical gold standards [14-15]. Recently, a large array of electrodes and statistical signal processing methodology, termed high-resolution electrogastrography (HR-EGG) [16], have been shown to detect gastric myoelectric dysfunction in common foregut disorders. Specifically, patterns from HR-EGG correlate with invasive measures [17] as well as symptom severity in patients with functional dyspepsia and gastroparesis [18]. It has also been shown that gastric slow wave parameters are distinct in healthy controls compared to patients with diabetic gastroparesis [19]. It was also recently shown that in children, spatiotemporal characterization of gastric slow wave activity using HR-EGG distinguishes symptomatic chronic nausea patients from healthy subjects [20]. Key opinion leaders have suggested that efforts be placed to confirm these findings in larger and more heterogeneous patient populations [21].

Although findings from HR-EGG show great promise, all prior works relied on placing individual electrodes on the skin overlying the stomach with precise electrode interdistances [16-18]. Furthermore, commercial electrodes are pregelled, which means that during continuous long-term recording, electrodes may dry and change their electrode–skin impedance which can result in inaccuracy of the reading.

Herein, we present a single stretchable adhesive-integrated multi-electrode array that enables continuous unobtrusive monitoring of the EGG. This patient-friendly, disposable peel-and-stick adhesive embedded device completely eliminates the challenges associated with a previous generation wearable EGG monitoring system [16-18]. Further, silver-silver chloride

(Ag/AgCl) as the electrode material of the sensor array alongside conformal contact with the human skin enables this class of flexible electronics to attain high signal-to-noise ratio (SNR) at the EGG frequency of 0.05 Hz.

Previously, this class of epidermal devices was successfully used to monitor fast-moving electrophysiologic signals, such as electroencepalogram (EEG), electrocardiogram (ECG) and electromyogram [22-24], using gold as the component of the electrode in contact with skin. Those signals typically have spectral components at frequencies of 1 Hz above. However, at lower frequencies, such as 0.05 Hz associated with EGG, the polarizable nature of gold or metal electrodes in general, creates an offset potential at the electrode–skin junction that will interfere with the under- lying slow electrophysiological signals of interest.

Since the signal of interest pertaining to EGG is 0.05 Hz, this implies that in this recording region, gold is very susceptible to DC noise. To elaborate, gold electrodes exhibit a high electrode–skin impedance, due to low ion mobility, which will form a barrier for the biopotential waveform to cross. On the flipside, Ag/AgCl electrodes are non-polarizable and allow for their Cl^- ion to partake in free charge exchange which eliminates charge buildup [25-26]. It has been established that for very slow frequencies (e.g., <1 Hz), Ag/AgCl exhibits very consistent and very low offset voltage, resistance, polarization, and drift, in comparison to variability in these parameters for gold and other metals [25-27].

Fabrication of stretchable electronics is typically performed using equipment associated with standard complementary metal-oxide semiconductor (CMOS) processes, such as thin film deposition, dry etching, and photolithography [22,24,28]. However, the type of materials that can be deposited in a clean room setting is very limited, and excludes Ag/AgCl. One possible approach

for fabricating stretchable Ag/AgCl electrode arrays involves post-clean room processes that include chlorination (e.g., dipping in ferric chloride ($FeCl_3$)) of exposed silver (Ag) film. However, performing this task with thin films that are sputter/electron beam-deposited present certain vulnerabilities to consistently produce low-impedance sensors that are mechanically robust. On the one hand, impedance decreases with thickness, but on the other hand, it is very challenging to produce a metal layer that is very thick (e.g., >1 μm) with a clean room deposition tool. The Ag film needs to be thick due to the chlorination process that converts most of the Ag into AgCl. In order for the sensor array to work as intended, a bilayer of Ag/AgCl is needed. Therefore, the film needs to be thick enough to leave the Ag component alongside the converted AgCl. AgCl film alone is very brittle, powdery, and has high impedance.

Further, the lack of process control in submerging a wafer with Ag film exposed in a chlorinated solution (e.g., $FeCl_3$) results in very low yield due to failure modes including film disintegration or electrodes with very high impedance (MΩ). Specifically, impedance of the AgCl layer depends on multiple factors, including thickness of Ag thin film deposited, the concentration of the $FeCl_3$ solution, as well as the amount of time that the Ag film is submerged inside the chlorinated solution. To elaborate more on the limitations, first, it is very challenging to produce an Ag layer that is very thick (e.g., >1 μm) with a clean room deposition tool. Second, the lack of process control pertaining to creation of the Ag/AgCl layer with the chlorination method often results in poor film quality (e.g., film becomes powdery and non-binding to the surface of the insulator beneath it). To be deemed usable, the Ag/AgCl film needs to be relatively uniform spatially, have a smooth surface, and have relatively low impedance. Given the limitation of depositing thick metal films with standard CMOS technology, it is sensible to explore printing methodologies to create reliable thick film layers for sensing applications [29-30].

In this study, we successfully combine a hybrid approach that merges thin film CMOS processing technology and thick film screen printing technology [31,32] to demonstrate the first successful flexible dry Ag/AgCl electrode arrays for EGG monitoring. Marrying the two techniques results in a device that is easily embedded in adhesive, disposable, and easy to apply.

Results

Wafer-level fabrication was carried out using standard CMOS procedures as outlined in the Experimental Section. **Figure 1.1**c shows the cleanroom-produced silicon wafer containing the sensor array prior to the screen printing process of the Ag/AgCl layer. This wafer was then screen-printed with Ag/AgCl ink using a 75 um thick standard stainless-steel stencil which yielded a 37.5 μm thick Ag/AgCl layer. The ink was solely printed on the active sensor area (ten circles of 8.6 mm diameter). The resulting device, including the Ag/AgCl layer, is shown in **Figure 1.1**d. Upon completion, the device was then transfer-printed using a water-soluble tape to a silicone (Ecoflex)/ silicone adhesive (Silbione) substrate as shown in **Figure 1.1**e.

We implemented an electrical impedance spectroscopy (EIS) procedure to determine the impedance of our electrodes across different frequencies. We immersed the electrodes in a 0.9% NaCl (154 mm) solution (physiological concentration which is isotonic to body fluids) to simulate the physiologic properties of human body fluids [33].

We ran EIS for three different types of electrodes, the standard 3M Red Dot that acted as a control, the Au flexible sensor (before screen-printed with Ag/AgCl), and the screen- printed Ag/AgCl flexible sensor. BioLogic SP-200 potentiostat (PEIS function) was used to sweep from 0.01 to 5 Hz and impedance was measured in units of Ω. Since a material's impedance is inversely

proportional to its surface area, we compared different electrodes of different surface areas with the area specific impedance (ASI) which was in the unit of $\Omega.mm^2$ [34].

It can be seen from **Figure 1.2**c that the general characteristic of decay in ASI with an increase in frequency is due in part to the inverse relationship between impedance and frequency in capacitive materials. It can be seen that the 3M Red Dot electrode had the lowest ASI at every single frequency point compared to the flexible Au and flexible Ag/AgCl sensors. This behavior was expected due to the fact that 3M Red Dot is a wet electrode with conductive gel, as well as the fact that the Ag/AgCl was bulk in thickness (e.g., not thin film). However, for low frequency domain, specifically from 0.01 to 0.6 Hz, Ag/AgCl flexible electrodes showed lower ASI than Au flexible electrodes. This behavior is expected because of aforementioned resistance, polarization, and drift challenges at low frequencies associated with Au electrodes [25,26]. Usage of different classes of Ag/AgCl inks, with different ratios of particle ingredients, may allow for optimization to further reduce impedance.

Once EIS characterization was performed, we proceeded to place the electrode array on the abdomen for data collection. It has been established that there is high variability in interindividual stomach location relative to visible skin-based landmarks for electrode placement (e.g., the xiphoid and umbilicus) [18]. Ultrasound is used to locate the antrum of the stomach for many purposes, including assessing gastric contents and volume [35]. Building upon this, we took advantage of a newly developed portable ultrasound system that can be interfaced with a mobile phone/tablet to enable fully ambulatory image- guided placement of the electrodes array over the antrum. A representative result of the ultrasound image for one patient could be seen on **Figure 1.3**a.

Ultrasound images for test subjects were gathered to verify the placement of the electrodes. The Butterfly IQ portable ultra- sound system was used to image the abdomen area of the subjects to locate the stomach location (setting: abdomen mode at 10 cm depth and 21–22 Hz frequency). Before imaging, the subject was asked to drink 8 oz of water, followed by the application of ultrasound gel to aid the imaging. Subjects were instructed to sit on a chair while leaning their backs against it. The ultra- sound transducer probe was lightly pressed against the subject's abdomen and swept vertically to locate the stomach. Subjects were instructed to lie sideways to get a secondary scan to increase sensitivity of stomach localization. After stomach localization, the electrode array was placed over the antrum (**Figure 1.3b**).

One human subject's electrode array and recording analyses are shown in **Figure 1.4**. Filtered waveforms from electrodes 1 through 4 are shown in Figure 4a. After performing artifact rejection algorithms tailored to EGG recordings [17], our methods as shown in Figure 4b represent a strong peak in the spectral representation of the processed signal at 0.053 Hz, near the gastric pacemaker frequency of 0.05 Hz that underlies the EGG. This spectrographic representation is comparatively superior to other findings of the literature that have prohibitive noise due to artifacts and other sources of noise [36]. The top of **Figure 4**c shows a spectrogram indicative of spectral power (in dB) at frequencies between 0 and 0.1 Hz across time. The bottom of Figure 4d shows normalized EGG (pertaining to the band of 0.03–0.07 Hz) which was defined as zero when below a statistically defined baseline (described in the Experimental Section). A large increase in normalized EGG power occurred and persisted ~10 min after the subject had a meal. The area under the curve (AUC) of the normalized EGG power in the 30-min postprandial (e.g., after meal consumption) interval exceeded that of the 30-min preprandial (e.g., before meal consumption) interval.

Across all ten subjects, the median peak in spectral power was 0.053 Hz with a standard deviation of 0.004 Hz. Further, the difference between 30-min postprandial AUC and 30-min preprandial AUC was statistically significant (one-sided *t*-test, $p < 0.05$). These results are showcased in **Figure 1.5**.

Discussion

We have demonstrated an unobtrusive adhesive-integrated flexible and stretchable multi-electrode array for continuous and non-invasive measurement of the neuromuscular activity of the stomach manifested in the EGG. Furthermore, we addressed the problems associated with long-duration recordings with wet electrode systems through this new class of adhesive-integrated electrodes that utilizes a combination of lithography-based technique as well as screen printing of dry Ag/AgCl ink. We have successfully eliminated the challenge of limited materials selection associated with the ordinary lithography-based technique. In order to address intersubject variability in stomach location, we have shown that dependence on volumetric imaging at a facility (e.g., a CT or MRI scan) can be replaced with the use of a portable handheld ultrasound system, at the time of electrode placement, that can be interfaced with a mobile device [18]. This successful integration of using an ultrathin adhesive-integrated multi-electrode array, guided with mobile imaging, increases the plausibility that highly accurate fully ambulatory neuromuscular GI monitoring is feasible.

Our observation of all subjects having normal gastric activity within the range of 2–4 cycles/min is consistent with other EGG findings in normative controls following meal consumption [37].

Patients with gastric disorders sometimes exhibit irregular neuromuscular activity that can include tachygastria (above 4 cycles/min) and bradygastria (below 2 cycles/min) [38,39]. The combination of our novel Ag/AgCl electrodes, which remove baseline drift, as well as the motion artifact rejection algorithm, which removes short bursts of high-amplitude activity, suggest that tachygastria can be captured with this approach. On the flipside, given that baseline drift is prone to occur during long- duration recordings, more evidence is needed to determine if this class of electrodes is robust to the detection of bradygastria for ambulatory recordings. Modern dynamic signal processing algorithms that utilize Bayesian inference, group sparsity, and multitaper methods may complement the optimization of future electrodes to yield further improvements [40-42].

The statistically significant increase in AUC of the normalized EGG power from preprandial 30-min windows to postprandial 30-min windows across the group of ten subjects is consistent with findings associated with meal consumption. Specifically, we expected an increase in sustained normalized EGG power since ingestion of food is known to active excitatory neural responses of the stomach that increase the force of gastric smooth muscle contractions, and since the strength of gastric contractions is associated with the magnitude of EGG waveforms [43-45]. It is plausible that future studies that involve ambulatory EGG monitoring with this technology may use features such as the AUC or time duration until postprandial-normalized EGG power returns to baseline, to determine associations with symptom severity in patients with upper GI disorders.

A logical next step to evolve this technology is to perform 24-h recordings in normal subjects and patients with GI disorders to understand the relationship between meals, EGG patterns, symptoms, and interventions such as medication(s). This is particularly relevant, as it is well

known that GI symptoms are transient and sometimes do not occur during a clinic visit. Moreover, development of a non-invasive EGG system allows for evaluation of specialized patient populations such as neonates, children, older adults, and pregnant women, groups who often experience GI symptoms but are ineligible for invasive testing. Opportunities to match symptom logs by patients with patterns from EGG waveforms may allow for modern machine learning techniques to aid GI specialists in disambiguating the causes of symptoms and optimize treatment regimens. It was recently shown that 90-min recordings with 25 individual electrodes interfaced to a conventional bulky amplification system allow for the extraction of spatial patterns from the high-resolution EGG that correlate with symptom severity [18].

While we have moved from a bulky wearable electronic device [17] to a flexible and stretchable electrode array, we have neither performed a 24 h recording with our electrode array nor recorded from a sufficient number of channels to extract spatial patterns. In such studies, it will be ideal to utilize miniaturized biopotential boards, such as the WAND Mini [46], the BioADC board [47], or the Intsy board [48] in an ambulatory study, in order to match the minimal invasiveness of the stretchable electrode array and record from 25 or more channel inputs to enable extracting spatial patterns. Since such an electrode array would be applied once to the skin and interfaced to a miniaturized board without long cables, significant noise reduction will ensue—further improving the ability to resolve spatial patterns.

The increasing attention being placed on slow electrical oscillations (<1 Hz) in the brain may allow for the use of these technologies in EEG recordings [27,49,50]. Further, recent efforts attempting to understand the electrophysiological interplay between the brain, autonomic nervous system, and stomach may allow for this class of sensors to be employed in joint EEG and EGG recordings [51,52].

Wearable ECG technology has generated significant improvements in detection of events and informing diagnosis and treatment response for cardiovascular disease [53,54]. The momentum to explore the use of technologies with telehealth more generally has only increased momentum due to the COVID-19 pandemic [55]. Technologies like those employed in this study may aid in minimizing the trade-off between patient comfort and signal integrity to allow for large datasets containing ambulatory EGG recordings and symptoms to be created in the com- fort of one's home. This has the potential to propel machine learning and decision-support technologies and allow for physicians to improve their diagnosis and treatment of GI disorders.

Experimental Section/Methods

Electrodes Array Fabrication:

A silicon wafer was cleaned with acetone, IPA, DI water, IPA followed by drying with N_2. It was then baked on a 180 °C hotplate to dry completely. The clean wafer was then spun-coated with polydimethylsiloxane at 4000 rpm which would act as a weakly adhering substrate for subsequent fabrication steps. Polyimide (HD Microsystems, Inc., Parlin, NJ) was spun-coated at 4000 rpm, followed by a soft bake of 110 °C for 1 min and 150 °C for 5 min, and a full hard in a N_2 rich environment oven at 300 °C. Polyimide acted as an insulator for the following metal sensors and interconnects. Metallization of 10 nm chrome and 250 nm gold was then followed (Temescal BJD 1800 E-Beam Evaporator, Livermore, CA). Standard microfabrication procedures (photolithography and metal wet etching) were performed to define sensors and interconnects. Another layer of polyimide was then spun-coated, soft-baked, and hard-baked with the same parameters as above. The polyimide was then patterned via photolithography and reactive ion etching with O_2 plasma to define the insulator layer. 37.5 μm silver/silver chloride ink, 50% solid

by volume (Creative Materials, Inc., Ayer, MA) was then deposited via screen printing (with 75 μm stainless steel stencil) onto the sensor areas. Water-soluble tape (3M, Inc., Saint Paul, MN) was then used to transfer-print the device from the silicon wafer to a polymethylmethacrylate-treated glass substrate (acted as a non-stick release layer) that was spun-coated at 3000 rpm with Ecoflex (Smooth On, Inc., Macungie, PA) which acted as a backbone silicone and Silbione RT Gel (Elkem, Inc., Brunswick, NJ) which acted as an adhesive silicone. A custom zero insertion force (ZIF) connector was then interfaced with the ten-electrode array using anisotropic tape which facilitated bonding (3M, Inc., Saint Paul, MN) by applying heat and pressure on the bonding sites.

Participants:

Cutaneous recordings were performed on ten healthy subjects: age: 21 ± 2 years (range: 19–25 years); BMI: 22 ± 2 (range: 19–24). Each subject was asked to fast prior to the start of the recording, for a duration of 90 min; 30 min preprandial and 60 min postprandial consumption. At the 30 min mark, a 250 kCal nutrient bar and 8 oz water was consumed by each participant.

Electrode Placement:

A portable ultrasound was performed to guide placement of the multi-electrode array over the antrum. Ultrasound gel was used during ultrasound imaging of the stomach. Abdomen mode at 10 cm depth and 21–22 Hz frequency was used.

The device was then applied to the abdomen and the glass substrate was subsequently peeled off. The other end of the ZIF connector was attached to an adapter board (Adafruit Industries, Inc., New York, NY) which was then connected via jumper cables to a biopotential board (OpenBCI, Inc.) along with ground and reference electrodes (3M Red Dot, 3M, Inc., Saint Paul, MN).

Data Collection:

After bonding with a custom connector, the device was then transferred to the abdomen where the stomach was located (verified using ultrasound via Butterfly IQ) and the glass substrate was subsequently peeled off (Figure 3c). The medical grade adhesive silicone enabled the device to attach conformally to the abdomen area. The other end of the ZIF connector was attached to an adapter board (Adafruit Industries, Inc., New York, NY) which was then connected via jumper cables to a Bluetooth biopotential board (OpenBCI, Inc.) along with ground and reference electrodes (3M Red Dot, 3M, Inc., Saint Paul, MN). Recording was performed and the data was streamed wirelessly to the OpenBCI GUI installed on a Microsoft Surface 3 computer (Microsoft, Inc., Redmond, WA). The choice of wireless biopotential data acquisition board was based on previously published findings that indicated adequate noise rejection and artifact rejection for ambulatory EGG monitoring using the same acquisition system [17].

Data Processing:

Signals from each electrode were recorded with the OpenBCI specifications pertaining to a gain of 24x, resulting in a scale factor of 0.02235 μV per count, and sampling rate of 250 Hz. After signals were down-sampling to 1 Hz, a finite impulse response filter was performed with pass-band frequencies between 0.015 and 0.15 Hz [16]. In order to eliminate movement related artifacts, an interference cancellation procedure was employed that used an interference cancellation procedure involving minimum mean squared estimation with locally estimated mean and variance statistics [17]. A short-time Fourier transform spectrogram with 75% overlap and Hamming window was implemented for each pair of measurement electrodes. SNR was defined as the average power (in dB) between 0.04 and 0.06 Hz subtracted from the average power in all other frequencies between 0.02 and 0.15 Hz [17]. The pair with highest SNR was identified and

performed subsequent statistics based upon the waveform defined from the highest SNR pair. Baseline power was calculated as 3 dB above the 98.5th percentile of the spectral power at frequencies above 0.07 Hz. Normalized EGG power was defined to be the power (in dB) calculated from the spectrogram between 0.03 and 0.07 Hz when it exceeded baseline power, and zero otherwise.

Human Experiment:

Data collection was done as part of an ongoing study at the University of California San Diego, whose institutional review board provided ethical approval (IRB number 141069 "A pilot trial to evaluate the utility of passive, skin-mounted electrodes to monitor the electrical activity of the human digestive system").

Acknowledgements

The authors would like to acknowledge useful discussions about electrode characterization from Prof. Shadi Dayeh. Further, the authors would like to acknowledge graphic design assistance from Crystal Doan. T.P.C acknowledges support from NSF grant BCS-1932619. This work was performed in part at the San Diego Nanotechnology Infrastructure (SDNI) of UCSD, a member of the National Nanotechnology Coordinated Infrastructure (NNCI), which is supported by the NSF grant ECCS-1542148.

This chapter, in full, is a reprint of the material as it appears in Advanced Materials Technologies, 2020. Jonas F. Kurniawan, Boris Tjhia, Vincent M. Wu, Andrew Shin, Nathan L. J. Sit, Timothy Pham, Andrew Nguyen, Carleen Li, Rajan Kumar, Marcelo Aguilar-Rivera, Imanuel

Lerman, David C. Kunkel, Todd P. Coleman. The dissertation author was the primary investigator of this material.

References

[1] Brun, R., & Kuo, B. (2010). Functional dyspepsia. *Therapeutic advances in gastroenterology*, *3*(3), 145-164.

[2] Gikas, A., & Triantafillidis, J. K. (2014). The role of primary care physicians in early diagnosis and treatment of chronic gastrointestinal diseases. *International journal of general medicine*, *7*, 159.

[3] Heetun, Z. S., & Quigley, E. M. (2012). Gastroparesis and Parkinson's disease: a systematic review. *Parkinsonism & related disorders*, *18*(5), 433-440.

[4] Horowitz, M., Su, Y. C., Rayner, C. K., & Jones, K. L. (2001). Gastroparesis: prevalence, clinical significance and treatment. *Canadian Journal of gastroenterology*, *15*(12), 805-813.

[5] Corinaldesi, R. V. C. E. R. L., Stanghellini, V., Raiti, C., Rea, E., Salgemini, R., & Barbara, L. (1987). Effect of chronic administration of cisapride on gastric emptying of a solid meal and on dyspeptic symptoms in patients with idiopathic gastroparesis. *Gut*, *28*(3), 300-305.

[6] McCallum, R. W., Cynshi, O., & Investigative Team. (2007). Clinical trial: effect of mitemcinal (a motilin agonist) on gastric emptying in patients with gastroparesis–a randomized, multicentre, placebo-controlled study. *Alimentary pharmacology & therapeutics*, *26*(8), 1121-1130.

[7] Barton, M. E., Otiker, T., Johnson, L. V., Robertson, D. C., Dobbins, R. L., Parkman, H. P., ... & Dukes, G. E. (2014). 70 A Randomized, Double-Blind, Placebo-Controlled Phase II Study (MOT114479) to Evaluate the Safety and Efficacy and Dose Response of 28 Days of Orally Administered Camicinal, a Motilin Receptor Agonist, in Diabetics With Gastroparesis. *Gastroenterology*, *5*(146), S-20.

[8] Abell, T. L., Kedar, A., Stocker, A., Beatty, K., McElmurray, L., Hughes, M., ... & Fraig, M. (2019). Gastroparesis syndromes: Response to electrical stimulation. *Neurogastroenterology & Motility*, *31*(3), e13534.

[9] Angeli, T. R., Cheng, L. K., Du, P., Wang, T. H. H., Bernard, C. E., Vannucchi, M. G., ... & Farrugia, G. (2015). Loss of interstitial cells of Cajal and patterns of gastric dysrhythmia in patients with chronic unexplained nausea and vomiting. *Gastroenterology*, *149*(1), 56-66.

[10] O'Grady, G., Angeli, T. R., Du, P., Lahr, C., Lammers, W. J., Windsor, J. A., ... & Cheng, L. K. (2012). Abnormal initiation and conduction of slow-wave activity in gastroparesis, defined by high-resolution electrical mapping. *Gastroenterology*, *143*(3), 589-598.

[11] Abell, T. L., Johnson, W. D., Kedar, A., Runnels, J. M., Thompson, J., Weeks, E. S., ... & Griswold, M. E. (2011). A double-masked, randomized, placebo-controlled trial of temporary endoscopic mucosal gastric electrical stimulation for gastroparesis. *Gastrointestinal endoscopy*, *74*(3), 496-503.

[12] Elmasry, M., Hassan, H., Atassi, H., Stocker, A., McElmurray, L., Cooper, K., ... & Abell, T. (2019). Mo1607–Baseline Predictive Factors for Fore and Hind Gut Response to Long-Term Gi Electrical Stimulation. *Gastroenterology*, *156*(6), S-798.

[13] Parkman, H. P., Hasler, W. L., Barnett, J. L., & Eaker, E. Y. (2003). Electrogastrography: a document prepared by the gastric section of the American Motility Society Clinical GI Motility Testing Task Force. *Neurogastroenterology & Motility*, *15*(2), 89-102.

[14] Koch, K. L., & Stern, R. M. (2003). *Handbook of electrogastrography*. Oxford University Press.

[15] Abid, S., & Lindberg, G. (2007). Electrogastrography: poor correlation with antro-duodenal manometry and doubtful clinical usefulness in adults. *World Journal of Gastroenterology: WJG*, *13*(38), 5101.

[16] Gharibans, A. A., Kim, S., Kunkel, D. C., & Coleman, T. P. (2017). High-resolution electrogastrogram: a novel, noninvasive method for determining gastric slow-wave direction and speed. *IEEE Transactions on Biomedical Engineering*, *64*(4), 807-815.

[17] Gharibans, A. A., Smarr, B. L., Kunkel, D. C., Kriegsfeld, L. J., Mousa, H. M., & Coleman, T. P. (2018). Artifact rejection methodology enables continuous, noninvasive measurement of gastric myoelectric activity in ambulatory subjects. *Scientific reports*, *8*(1), 1-12.

[18] Gharibans, A. A., Coleman, T. P., Mousa, H., & Kunkel, D. C. (2019). Spatial patterns from high-resolution electrogastrography correlate with severity of symptoms in patients with functional dyspepsia and gastroparesis. *Clinical Gastroenterology and Hepatology*, *17*(13), 2668-2677.

[19] Bradshaw, L. A., Cheng, L. K., Chung, E., Obioha, C. B., Erickson, J. C., Gorman, B. L., ... & Richards, W. O. (2016). Diabetic gastroparesis alters the biomagnetic signature of the gastric slow wave. *Neurogastroenterology & Motility*, *28*(6), 837-848.

[20] Somarajan, S., Muszynski, N. D., Olson, J. D., Comstock, A., Russell, A. C., Walker, L. S., ... & Bradshaw, L. A. (2021). The effect of chronic nausea on gastric slow wave spatiotemporal dynamics in children. *Neurogastroenterology & Motility*, *33*(5), e14035.

[21] Hasler, W. L. (2020). Targeting Treatment of Gastroparesis: Use of Clinical Tests to Guide Treatments. *Gastroenterology Clinics*, *49*(3), 519-538.

[22] Kim, D. H., Lu, N., Ma, R., Kim, Y. S., Kim, R. H., Wang, S., ... & Yu, K. J. (2011). Epidermal electronics. *science*, *333*(6044), 838-843.

[23] Chung, H. U., Kim, B. H., Lee, J. Y., Lee, J., Xie, Z., Ibler, E. M., ... & Ogle, C. (2019). Binodal, wireless epidermal electronic systems with in-sensor analytics for neonatal intensive care. *Science*, *363*(6430), eaau0780.

[24] Xu, B., Akhtar, A., Liu, Y., Chen, H., Yeo, W. H., Park, S. I., ... & Jung, S. (2016). An epidermal stimulation and sensing platform for sensorimotor prosthetic control, management of lower back exertion, and electrical muscle activation. *Advanced Materials*, *28*(22), 4462-4471.

[25] P. Tallgren, S. Vanhatalo, K. Kaila, and J. Voipio, "Evaluation of commercially available electrodes and gels for recording of slow EEG potentials," Clin. Neurophysiol., vol. 116, no. 4, pp. 799–806, 2005.

[26] Albulbul, A. (2016). Evaluating major electrode types for idle biological signal measurements for modern medical technology. *Bioengineering*, *3*(3), 20.

[27] P. Tallgren, S. Vanhatalo, K. Kaila, and J. Voipio, "Evaluation of commercially available electrodes and gels for recording of slow EEG potentials," Clin. Neurophysiol., vol. 116, no. 4, pp. 799–806, 2005.

[28] Kim, Y. S., Lu, J., Shih, B., Gharibans, A., Zou, Z., Matsuno, K., ... & Tolley, M. T. (2017). Scalable manufacturing of solderable and stretchable physiologic sensing systems. *Advanced Materials*, *29*(39), 1701312.

[29] Tian, B., Yao, W., Zeng, P., Li, X., Wang, H., Liu, L., ... & Wu, W. (2019). All-printed, low-cost, tunable sensing range strain sensors based on Ag nanodendrite conductive inks for wearable electronics. *Journal of Materials Chemistry C*, *7*(4), 809-818.

[30] Kumar, R., Shin, J., Yin, L., You, J. M., Meng, Y. S., & Wang, J. (2017). All-printed, stretchable Zn-Ag2O rechargeable battery via hyperelastic binder for self-powering wearable electronics. *Advanced Energy Materials*, *7*(8), 1602096.

[31] Mohan, A. V., Kim, N., Gu, Y., Bandodkar, A. J., You, J. M., Kumar, R., ... & Wang, J. (2017). Merging of Thin-and Thick-Film Fabrication Technologies: Toward Soft Stretchable "Island–Bridge" Devices. *Advanced Materials Technologies*, *2*(4), 1600284.

[32] Bandodkar, A. J., You, J. M., Kim, N. H., Gu, Y., Kumar, R., Mohan, A. V., ... & Parthasarathy, M. (2017). Soft, stretchable, high power density electronic skin-based biofuel cells for scavenging energy from human sweat. *Energy & Environmental Science*, *10*(7), 1581-1589.

[33] Tonog, P., & Lakhkar, A. D. (2019). Normal saline.

[34] Klett, M., Gilbert, J. A., Pupek, K. Z., Trask, S. E., & Abraham, D. P. (2016). Layered oxide, graphite and silicon-graphite electrodes for lithium-ion cells: effect of electrolyte composition and cycling windows. *Journal of The Electrochemical Society*, *164*(1), A6095.

[35] Perlas, A., Chan, V. W., Lupu, C. M., Mitsakakis, N., & Hanbidge, A. (2009). Ultrasound assessment of gastric content and volume. *Anesthesiology: The Journal of the American Society of Anesthesiologists*, *111*(1), 82-89.

[36] Liang, J., Cheung, J. Y., & Chen, J. D. Z. (1997). Detection and deletion of motion artifacts in electrogastrogram using feature analysis and neural networks. *Annals of Biomedical Engineering*, *25*(5), 850-857.

[37] Lin, X., Levanon, D., & Chen, J. D. Z. (1998). Impaired postprandial gastric slow waves in patients with functional dyspepsia. *Digestive diseases and sciences*, *43*(8), 1678-1684.

[38] Chen, J., & McCallum, R. W. (1991). Electrogastrography: measurement, analysis and prospective applications. *Medical and Biological Engineering and Computing*, 29(4), 339-350.

[39] Koch, K. L. (2001). Electrogastrography: physiological basis and clinical application in diabetic gastropathy. *Diabetes technology & therapeutic*s, 3(1), 51-62.

[40] Kim, S., Quinn, C. J., Kiyavash, N., & Coleman, T. P. (2014). Dynamic and succinct statistical analysis of neuroscience data. *Proceedings of the IEEE*, 102(5), 683-698.

[41] Schamberg, G., Ba, D., & Coleman, T. P. (2018). A modularized efficient framework for non-Markov time series estimation. *IEEE Transactions on Signal Processing*, 66(12), 3140-3154.

[42] Kim, S. E., Behr, M. K., Ba, D., & Brown, E. N. (2018). State-space multitaper time-frequency analysis. *Proceedings of the National Academy of Sciences*, 115(1).

[43] Won, K. J., Sanders, K. M., & Ward, S. M. (2005). Interstitial cells of Cajal mediate mechanosensitive responses in the stomach. Proceedings of the National Academy of Sciences, 102(41), 14913-14918.

[44] Yin, J., & Chen, J. D. (2013). Electrogastrography: methodology, validation and applications. *Journal of neurogastroenterology and motility*, 19(1), 5.

[45] Shimada, Y., Watanabe, M., Shibahara, N., Kita, T., Itoh, T., & Terasawa, K. (1998). Electrogastrographic power ratio in humans is not related to changes in antrum-skin distance but to antral motility. *Journal of gastroenterology*, 33(3), 310-317.

[46] Zhou, A., Santacruz, S. R., Johnson, B. C., Alexandrov, G., Moin, A., Burghardt, F. L., ... & Muller, R. (2019). A wireless and artefact-free 128-channel neuromodulation device for closed-loop stimulation and recording in non-human primates. *Nature biomedical engineering*, *3*(1), 15-26.

[47] Kim, C., Joshi, S., Courellis, H., Wang, J., Miller, C., & Cauwenberghs, G. (2018). Sub-$\mu $ V rms-Noise Sub-$\mu $ W/Channel ADC-Direct Neural Recording With 200-mV/ms Transient Recovery Through Predictive Digital Autoranging. *IEEE Journal of Solid-State Circuits*, *53*(11), 3101-3110.

[48] Erickson, J. C., Hayes, J. A., Bustamante, M., Joshi, R., Rwagaju, A., Paskaranandavadivel, N., & Angeli, T. R. (2018). Intsy: a low-cost, open-source, wireless multi-channel bioamplifier system. *Physiological measurement*, *39*(3), 035008.

[49] Khader, P., Schicke, T., Röder, B., & Rösler, F. (2008). On the relationship between slow cortical potentials and BOLD signal changes in humans. *International Journal of Psychophysiology*, *67*(3), 252-261.

[50] Stephen, E. P., Hotan, G. C., Pierce, E. T., Harrell, P. G., Walsh, J. L., Brown, E. N., & Purdon, P. L. (2020). Broadband slow-wave modulation in posterior and anterior cortex tracks distinct states of propofol-induced unconsciousness. *Scientific reports*, *10*(1), 1-11.

[51] Levinthal, D. J., & Strick, P. L. (2020). Multiple areas of the cerebral cortex influence the stomach. *Proceedings of the National Academy of Sciences*, *117*(23), 13078-13083.

[52] Azzalini, D., Rebollo, I., & Tallon-Baudry, C. (2019). Visceral signals shape brain dynamics and cognition. *Trends in Cognitive Sciences*, *23*(6), 488-509.

[53] Zimetbaum, P. J., & Josephson, M. E. (1999). The evolving role of ambulatory arrhythmia monitoring in general clinical practice. *Annals of Internal Medicine*, *130*(10), 848-856.

[54] Turakhia, M. P., Hoang, D. D., Zimetbaum, P., Miller, J. D., Froelicher, V. F., Kumar, U. N., ... & Heidenreich, P. A. (2013). Diagnostic utility of a novel leadless arrhythmia monitoring device. *The American journal of cardiology*, *112*(4), 520-524.

[55] Whitelaw, S., Mamas, M. A., Topol, E., & Van Spall, H. G. (2020). Applications of digital technology in COVID-19 pandemic planning and response. *The Lancet Digital Health*.

Figures

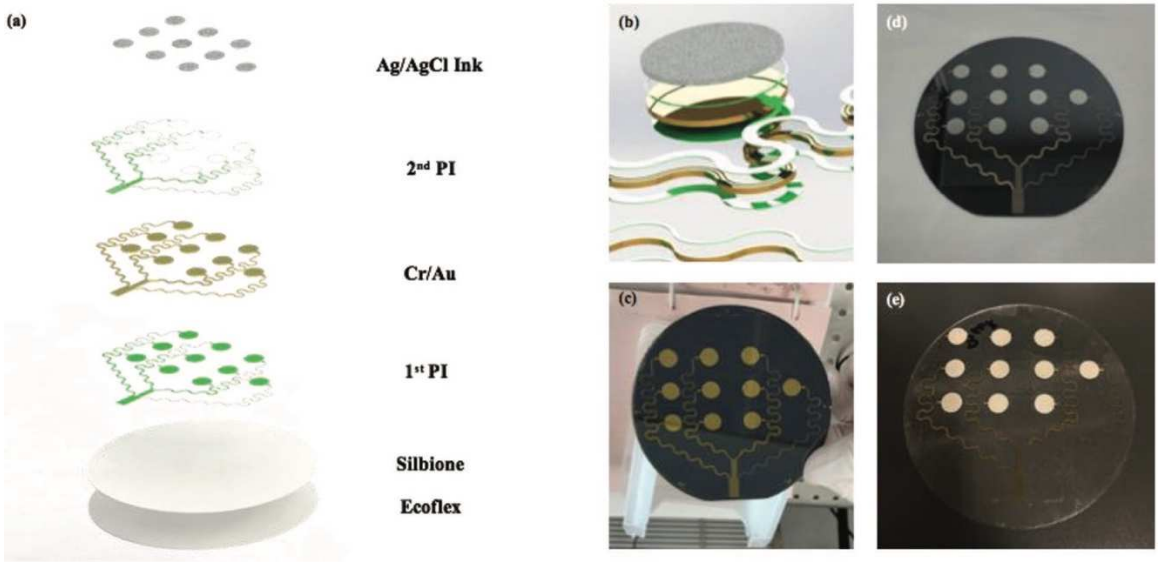

Figure 1.1. (a) Cross section of the entire device (86 mm sensor diameter and 200 um interconnect width). **(b)** Close-up cross section of the sensor layer, consisting of the bottom PI layer, Au, PI mesh, and Ag/AgCl printed layer. **(c)** Finished EGG device fabricated on a silicon wafer with Au on top layer before the screen printing process of Ag/AgCl has begun. **(d)** EGG device screen-printed with Ag/AgCl ink on the active sensor area (37.5 μm). **(e)** EGG device transferred into a flexible self-adhering silicone surface via water-soluble tape; the adhesive-integrated sensor array is now ready to be placed on the abdomen.

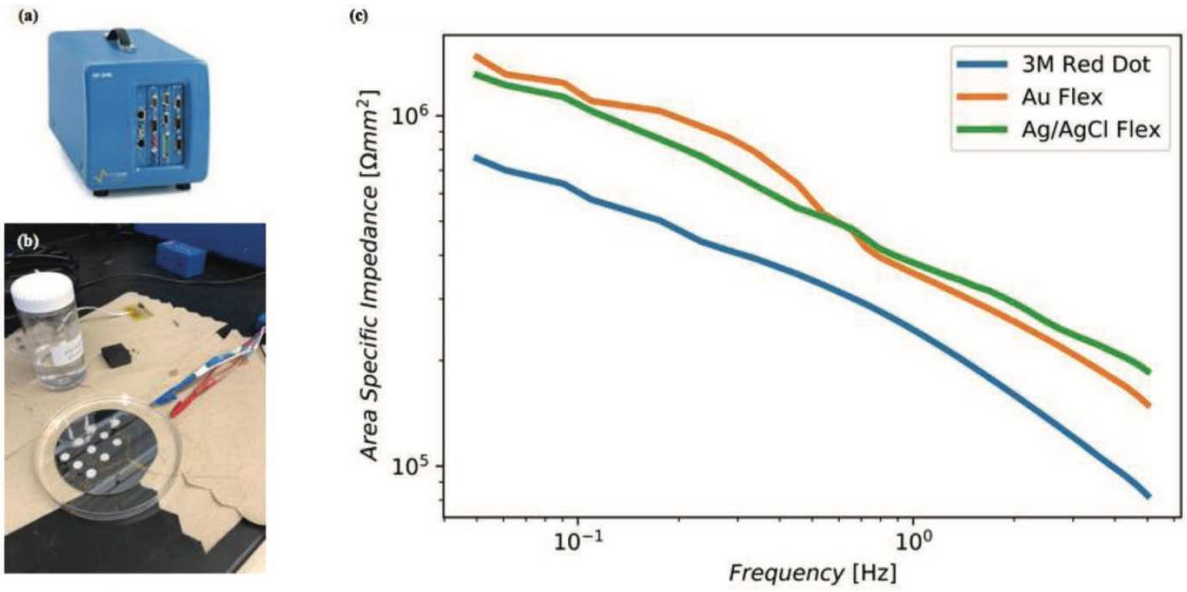

Figure 1.2. (a) BioLogic SP-200 potentiostat used to gather measurements of electrochemical impedance spectroscopy (EIS). **(b)** The sensor was connected to the positive (+) lead of the potentiostat; meanwhile, the negative (−) terminal of the potentiostat was connected to the NaCl solution via a metal header pin. The data were captured using PEIS function (potentiostatic EIS, where voltage is changed and current is measured). **(c)** EIS data for multiple electrode types is shown. The graph displays area specific impedance (ASI) variation as frequency changes from 0.01 to 5 Hz for 3M Red Dot (commercial), Au flexible electrodes (before Ag/AgCl screen printing), as well as the Ag/AgCl flexible electrodes. The ASI of Ag/AgCl flexible electrodes is lower than that of Au flexible electrodes for frequencies between 0 and 0.6 Hz, which includes the EGG frequency of 0.05 Hz.

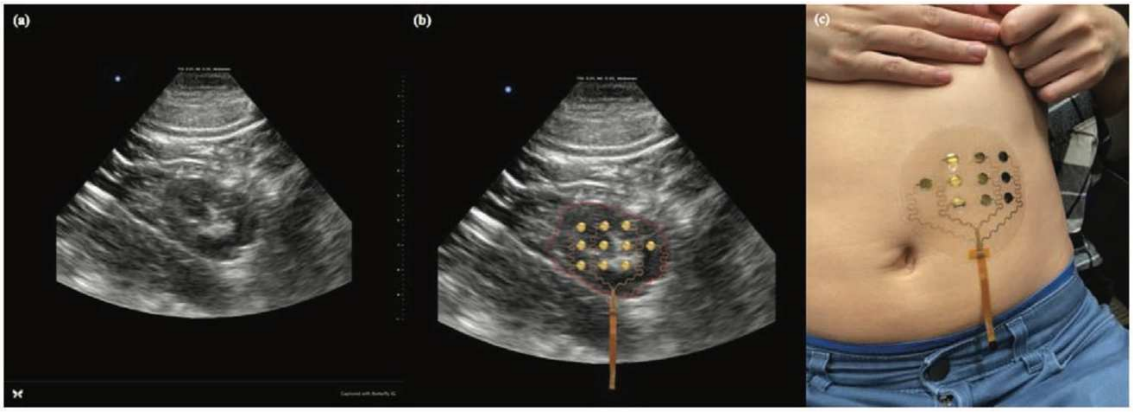

Figure 1.3. (a) Coronal ultrasound image of the stomach location of one subject which was used to guide the placement of electrodes. **(b)** Electrodes image was overlaid to the ultrasound image of stomach antrum to visualize the alignment of the electrode array to the stomach. These images were obtained using Butterfly IQ portable ultrasound system. **(c)** Electrodes array was placed directly on top of the stomach location that was found previously using the ultrasound image.

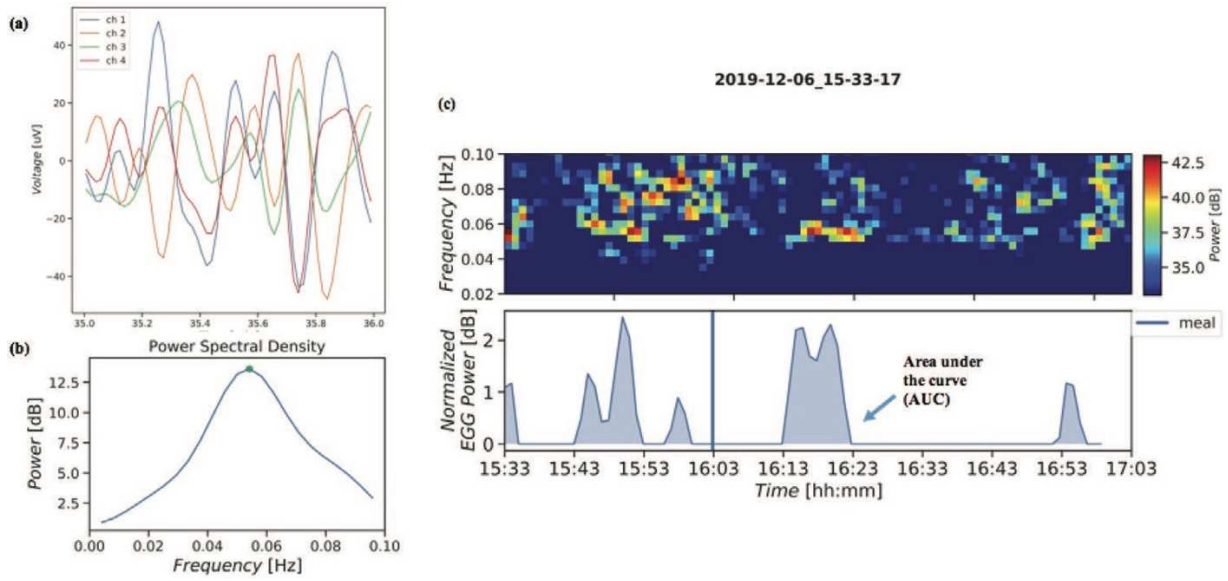

Figure 1.4. (a) Recording data showing four out of the eight channels electrodes array. Slight shift of the signals is suggestive that the wave was propagating. Band pass filtering was done between 0.01 and 0.1 Hz to filter out ECG and other fast moving signals. **(b)** Spectral representation of the signal from one electrode indicated a clear peak at 0.053 Hz. **(c)** Spectrogram from one electrode indicated high energy around 0.05 Hz (indicative of EGG signals) that started around 3:43 PM (preprandial), 4:03 PM (meal), and 4:13 PM (postprandial). Large areas under the curve and red spectrogram were indicative of clear gastric signals.

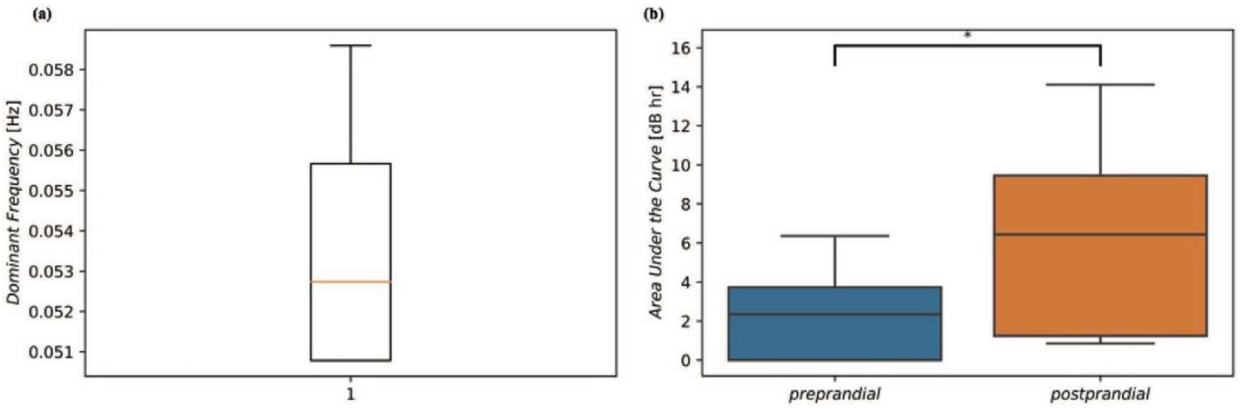

Figure 1.5. (a) A box plot indicative of median peak in spectral power of 0.0527 Hz, and 25th to 75th interquartile range spanning from 0.051 to 0.0555 Hz. **(b)** A box plot of area under the curve (AUC) for 30-min preprandial and postprandial intervals. A statistically significant increase from preprandial to postprandial AUC was found.

Chapter 2. Electrochemical Performance Study of Ag/AgCl and Au Flexible Electrodes for Unobtrusive Monitoring of Human Biopotentials

Abstract

Here, we investigated the electrochemical performance of various dry flexible electrodes, namely gold and silver/silver chloride. The electrochemical impedance spectroscopy (EIS) technique was used to understand the behavior of various electrode materials across different diameters and frequencies. Further, a simple circuit model was built to confirm the impedance behaviors of our electrodes. We then compared our results to the result obtained from the 3M RedDot electrode which acted as a control electrode. This study implied that silver/silver chloride performed much better at low frequencies (< 1 Hz) compared to Au and therefore should be the material of choice for electrophysiological recordings in that frequency range. At high frequency range (1 - 1000 Hz), Au and Ag/AgCl had similar performance. The study aims to enable future design of flexible electrodes for various biopotential recordings by allowing a systematic fine-tune of its material and size.

Keywords: flexible electronics, electrode array, electrophysiology, biopotential, electrochemical impedance spectroscopy (EIS).

Introduction

Flexible and stretchable electronics for recording body biopotentials have become more prevalent since the development of the first epidermal electronics systems [1]. In addition to being more comfortable for the patient to wear during the recording process, these electronics provide good signal fidelity across a broad frequency range. Flexible and stretchable electrode arrays are used for electroencephalogram (EEG) up to 100 Hz [2,3] and as low as sub hertz to capture the electrogastrogram (EGG) at 0.05 Hz [4,5,6,7]. This class of electronics holds tremendous potential for the advancement of healthcare.

The majority of studies involving stretchable electrodes are focused on capturing higher frequency signals such as those from the electrocardiogram (ECG), electromyogram (EMG), and EEG. As a result, these electrode arrays tend to be composed of metals like gold (Au) and platinum (Pt) [8,9,10,11]. In general, Au and Pt are classified as polarizable electrodes, which creates an offset potential at the electrode-skin interface. These materials also exhibit high electrode-skin impedance due to their low ion mobility, creating a barrier for the biopotential signals to cross. At higher frequencies, this barrier is minimized, however for low frequency recording these materials are not suitable.

A simple two-element circuit model can be used to describe the relationship between the electrolyte/interface/electrode. In the model, $R_{electrode}$ is defined as the sum of R_e (electrolyte resistance) in series with the R_i (interface resistance). R_i can be further defined as the parallel connection between Z_f (faradaic impedance) and C_d (double-layer capacitance). The dominant model elements are R_e and C_d. At a very high frequency (> 10 kHz), C_d shunts all the current, therefore the $R_{electrode}$ is approximately the same as R_e. Meanwhile, at a very low frequency (< 0.1 Hz), C_d becomes an open circuit and therefore the electrode impedance will be the sum of R_e and

R_i. At a medium frequency, impedance is defined as $1/j.\omega.C$. Therefore, in general as frequency of the signal increases, the impedance of the electrode will decrease [12,13].

For EEG, and ECG, because the target frequencies are higher, the choice of Au or Pt electrodes is sufficient. However, to record low frequency (i.e: EGG at 0.05 Hz), Au/Pt are susceptible to DC noise [7,14,15] and, based on the model, increased impedance which results in noisy recordings that contain baseline drift. Silver/silver chloride (Ag/AgCl) electrodes belong to a class of non-polarizable electrodes. Generally, for a non-polarizable electrode, the component Z_f will have a zero resistance. Therefore, the impedance of the electrode is approximated by the impedance of the electrolyte (Z_e). Therefore, the Ag/AgCl electrode will have a higher signal-to-noise ratio across all frequency ranges, but it will be particularly useful in capturing low frequency signals which are often corrupted by DC noise. Specifically, the Cl^- ion partakes in free charge exchange which eliminates charge build up on the electrode interface [7,14,15]. Further, the Ag/AgCl electrode exhibits very low offset voltage and baseline drift, making it an ideal choice of material for recordings in the low frequencies domain.

Previously, a study to classify the electrochemical performance of Au/Pt in electrocochleography (ECoG) electrodes was done [8,9]. However, in the study, the author targeted ECoG recording at higher frequencies (> 8 Hz for various alpha theta and gamma bands). So far, no characterization study has been done for the use of Ag/AgCl flexible electrodes on low frequency signals such as EGG. Therefore, in order to build a flexible electrode array which is of sufficient density for gastric inverse mapping [5,16] without reducing electrochemical performance, the AgAgCl electrodes need to be characterized across frequency and diameter. Previously, the authors successfully utilized a novel fabrication method to create flexible Ag/AgCl electrodes for EGG recording [7], however no characterization study has been done to investigate

the effect of diameter and frequency on the electrochemical performance of such electrodes. In this study we aim to provide the groundwork for future research into the use of Ag/AgCl electrodes.

Here, we utilized a potentiostat and a petri dish modified to support a metal header pin which made contact with a standard electrophysiologic 0.9% NaCL solution in the dish. We placed the Ag/AgCl or Au wafer in the dish and used galvanostatic electrochemical impedance spectroscopy (GEIS) to measure the complex impedance of each electrode. The electrochemical performance of these electrodes was benchmarked against the standard 3M RedDot electrode. We measured the complex impedance of each electrode (d = 1-10 mm) across a broad frequency range (0-1kHz).

Ultimately the goal of this study is to provide critical information for future optimization of flexible and stretchable electrode arrays. These results will allow the design process to utilize various constraints such as electrode size, desired impedance, and target frequencies to optimize recording quality. An array can now be built that is high density without sacrificing electrochemical performance. For example, two applications where flexible and stretchable electronics have been used are for measuring the neuronal activity of the vagus nerve [17,18] and the non-invasive recording of the gastric slow wave [7]. Electrode arrays for the vagus nerve require a smaller footprint to capture neuron cluster activities but also require small impedances (< 10 kOhm). Tracking the gastric slow wave, on the other hand, requires a spatially dense array of larger electrodes.

Results

Wafer-level fabrication was performed using standard CMOS procedures in a cleanroom environment, as outlined in the Experimental section. **Figure 2.1**a shows the cross section of the wafer for the EIS process. Although the electrodes were not transferred from the Silicon wafer to a silicone flexible substrate, to ensure an accurate impedance measurement, the selection of materials and layers was chosen to mimic flexible electrode fabrication steps. Post cleanroom processing, Ag/AgCl ink was screen printed using a standard 75 um thick stainless-steel stencil which yielded a 37.5 um dry layer of Ag/AgCl aftercuring. The ink was printed on the active sensor area (8 circles, with diameter of 1, 1.25, 2.5, 4, 5, 7.5, 8.6, and 10 mm). Upon screen printing, the electrodes were soldered with 0.20 mm diameter wire on the bonding pad and secured with 5-minute epoxy adhesive to insulate the pad. The experimental setup for the electrical impedance spectroscopy (EIS) experiment is shown in **Figure 2.1**d, where the electrode of interest was connected to the positive terminal (red) and the electrolyte was connected to the negative terminal (blue) of the BioLogic SP-200 potentiostat (**Figure 2.1**c).

The impedance of our Au and Ag/AgCl flexible arrays, as well as the 3M Red Dot electrodes (for a control) was measured using galvanostatic electronic impedance spectroscopy (GEIS) with a current of 100uA. Frequencies were swept from 0.01 to 0.99 Hz for low band and 1 to 1,000 Hz for high band. During the experiment, the electrodes were immersed in a 0.9% NaCl (154mM) solution (physiological concentration - isotonic) to simulate the physiologic properties of the human body [19]. Impedance was measured in the unit of Ω. We implemented area specific impedance (ASI) in the unit of $\Omega.mm^2$ to compare different electrodes of different surface area and materials (**Figure 2.5**) [20].

The impedance results from the experiment for Au and Ag/AgCl at 0.05 Hz (the frequency of interest for EGG) is plotted against electrode diameter (**Figure 2.2**) which yields graphs of |Z| vs electrode diameter for both materials. Custom fitting of |Z| vs diameter based on the derivation of the simple circuit model was performed for both materials and our findings were consistent with previous results from our previous paper [7] that impedance decreases as the area of the electrodes increases. Further, our fit model allows for extrapolating magnitude impedance as a function of electrode diameter. This model will future systematic electrode design (diameter and material) for EGG applications.

It can be seen from both plots (**Figure 2.2**), that in general the magnitude impedance for Au is higher than that of Ag/AgCl at 0.05 Hz frequency. This behavior is expected due to the resistance, polarization, and baseline drift associated with Au electrodes at low frequencies [7,14,15].

The magnitude impedance is plotted versus frequency on a semi log scale for each of the different electrode diameters, frequency bands, and materials. Au results are displayed in **Figure 2.3** and Ag/AgCl are displayed in **Figure 2.4**. The results for both low and high bands of Au were consistent across frequency range, namely the magnitude impedance decreases as frequency increases. This is due to the fact that impedance is inversely proportional to the frequency in the simple circuit model. The trend across diameters is also somewhat consistent with the theory that magnitude impedance decreases as diameter increases. This is mainly contributed to the fact that as diameter increases (increase in area), the capacitance term of the electrode increases, thus decreasing the overall impedance. However, in the Au low band 5 mm electrode had lower impedance than that of 8.6 mm electrode but higher than that of 10 mm electrode. Similarly, in the high band 5 mm and 4 mm electrodes had the lowest impedance, even lower than that of 10 mm.

Similarly, for Ag/AgCl the results for both low and high bands were consistent, just like Au electrodes, with the fact that as frequency increases, the magnitude impedance decreases. In general, the magnitude impedance results for Ag/AgCl were lower across the board as compared to Au electrodes. In the low band, most of the electrodes were behaving as expected across diameters, with an exception of the 8.6 mm diameter electrode having lower impedance than that of the 10 mm electrode. In the high band, 2.5 mm, 7.5 mm, and 8.6 mm electrodes had lower magnitude impedance than that of a 10 mm diameter electrode. These anomalous results across diameter trends both in Au and Ag/AgCl electrodes could be attributed to experimental and human errors. Sources of errors include the non-uniform application of solder to the pads and the wire, cold solder joints, and clamping force for the electrode wire to the potentiostat.

A comparison across different materials was performed as indicated by **Figure 2.5**. Here, the Au and Ag/AgCl flexible electrodes were benchmarked against the control 3M RedDot electrodes. ASI is used to compare the performance of each of the materials. We chose 8.6 mm diameter electrodes for the comparison due to the fact that 3M RedDot has an Ag/AgCl diameter (8.7 mm) close to our sensor diameter. For normalization, we used the area of the whole conductive layer of the 3M RedDot (955 mm^2). Across the low band, 3M RedDot had the highest ASI across all frequencies, followed by Au and Ag/AgCl. Further, for the high band, again 3M RedDot had the highest ASI across all frequencies with Ag/AgCl and Au being lower and showed very close results across multiple frequencies. The high ASI of 3M RedDot is expected because it has a very large surface area (almost 16x larger than our flexible electrodes).

Lastly, to compare the variability between wafers for both Au and Ag/AgCl flexible electrodes, we looked at ASI vs frequency for the 4 mm and 8.6 mm diameter electrodes in low and high bands. It can be seen in **Figure 2.6** that Ag/AgCl had more consistent results wafer to

wafer with very little variability across both diameters and frequencies. Meanwhile, Au showed more variability wafer to wafer, especially at the low band. At the high band, the results for Au were very similar in variability to Ag/AgCl for 8.6 mm and for 4 mm, it had more variability compared to AgAgCl. 4 mm diameter was chosen as it is a diameter of interest to build electrodes for other applications such as to capture the neuronal activities of the vagus nerve and 8.6 mm diameter was chosen as it is a diameter very close to the Ag/AgCl component (0.87 mm) of a 3M Red Dot control electrode.

Discussion

We have performed an electrochemical performance study for flexible electrodes for Au and Ag/AgCl at both low and high frequency bands. Frequency bands were selected due to the significance of their clinical applications, non-invasive measurement of stomach electrical activity is done using electrogastrogram (EGG) at 0.05 Hz [5,7], electrocardiogram (ECG) is performed at 0.05 - 150 Hz, electromyogram (EMG) contains frequencies up to 400 Hz, and surface neuronal activity is high frequency up to 1,000 Hz [18].

The characterization of various flexible electrodes has been performed mostly in the high frequency band [8,9] for the purpose of electrocorticography (ECoG) recording. We are hopeful that by performing this study, future design of electrodes for various biopotential recordings can be done systematically. For instance, the vagus nerve is a very thin and long nerve on the neck and it requires a small electrode diameter to be able to record its activity without recording the neighboring nerve activity. However, since the signal from the vagus nerve is not very strong, it is crucial that the electrodes have low impedance electrodes. On the other hand, having a dense array with greater electrode diameter is a requirement for the analysis of the gastric slow wave. Therefore,

having performed this study, we are able to predict the relationship between the material selection, diameter, as well as its impedance when designing future electrodes for different applications.

Area specific impedance (ASI) was used for the purpose of comparing different materials across different diameters. The impedance was multiplied by the area of each electrode to normalize the results of the impedance. Bigger area of electrodes will allow for smaller electrode impedance due to the fact that higher surface area electrodes will yield higher capacitance, and impedance is inversely proportional to the capacitance of the electrode. Our findings were consistent that across low frequency bands at all diameters, the magnitude impedance for Ag/AgCl is lower than that of Au flexible electrodes. However, in the high band the results were similar in magnitude impedance for both electrode materials. This implies that Ag/AgCl should be the material of choice for low frequency recording such as EGG due to its low impedance, as well as the non-polarizable nature of the materials which will prevent excess charge build up and baseline drift.

On the other hand, if one is designing an electrode array for high frequency recording (i.e: ECG, EMG, ECoG), gold should suffice as the material of choice. Our study proved that at high frequency, Au performed very similarly to Ag/AgCl. Therefore, when designing electrodes for higher frequencies recording, Au should suffice. Furthermore, it will save processing cost and time for not having to screen print Ag/AgCl.

Further, wafer-to-wafer variability was also studied by repeating the experiment across two different wafers. The variability was more prominent in Au flexible electrodes as compared to Ag/AgCl due to the fact that Au electrodes were only at the nanometer scale (250 nm), meanwhile, Ag/AgCl was at the micrometer scale (37.5 um). Therefore, small inconsistencies in processing such as during metal deposition will result in different thickness of gold, causing different

impedance values. Meanwhile, for Ag/AgCl, since it is at the micrometer scale, small inconsistency of thickness should not have a significant effect on the impedance value.

Further, wafer-to-wafer variability could also be attributed to two reasons, namely, the soldering of the wires, as well as the contact resistance between the electrode's wire and the clamp of the positive terminal (clamping force differed from wire to wire). With manual soldering, the amount of solder applied on the pads and on the wire might not be consistent across all electrodes from wafer-to-wafer. It's also possible that the higher impedance values could also be attributed to cold solder joints which in general will have worse electrical performance [21]. Additionally, at higher frequencies, although there was more degree of variability for Au compared to Ag/AgCl, the results for Au were more consistent in terms of variability compared to the low frequencies results. This is attributed to the fact that at high frequencies, based on the model, the frequency term contributed largely to the impedance term, helping the inconsistency that can arise from the material itself.

Overall, we have demonstrated a systematic way of studying the electrochemical performance of various Au and Ag/AgCl flexible electrodes across multiple different diameters and frequencies. It is the hope that for future research involving biopotential recordings can benefit from this study as it will allow the systematic selection of material and electrode diameter for given target impedance and frequencies.

Experimental Section/Methods

Electrodes Fabrication:

A 4" silicon wafer was pre-cleaned with acetone, IPA, DI water, IPA followed by drying with N_2 gun. The wafer was then baked at 180°C on a contact hotplate to remove remaining

moisture for 5 minutes. Polydimethylsiloxane (PDMS) which would act as a weakly adhering substrate was spun coated at 4000 rpm. Subsequently, Polyimide (HD Microsystems, Inc. - Parlin, NJ) was spun coated at 4000 rpm followed by a soft bake at 110°C for 1 min and at 150°C for 5 min on a contact hotplate to evaporate the solvent away. The wafer was then hard baked in a N_2 rich environment oven at 300°C for 2 hours. Metalization of 10nm chrome and 500 nm gold was then followed via an electron beam evaporator (Temescal BJD 1800 E-Beam Evaporator - Livermore, CA). Sensors with various diameters (10 mm, 8.6 mm, 7.5 mm, 5 mm, 4 mm, 2.5 mm, 1.25 mm, and 1 mm) were then patterned via standard lithographic procedures followed by wet etching to define the gold and chrome layer. Another layer of polyimide was spun coated using the same parameters as above. Photolithography and reactive ion etching (RIE) with O_2 plasma were used to define the bottom and top polyimide layer which acted as insulators. For some of the wafers, silver/silver chloride (Creative Materials, Inc. - Ayer, MA) was screen printed on the active sensor areas with a 75 um stainless steel stencil (Metal Etch Services, Inc - San Marcos, CA). A 0.20 mm wire was soldered to the bonding pad of each electrode. The bonding pad was then sealed using a Devcon 5-minute epoxy (ITW Performance Polymers - Danvers, MA) and the other end of the wire was tinned to allow conduction.

Data Collection:

Data recording was done using the BioLogic SP-200 instrument. Galvanostatic (GEIS) mode of measurement was used for the measurement of the electrochemical impedance spectroscopy (EIS) with current amplitude (I_a) of 100 uA. Each run was divided into two bands, the “low” band and the “high” band. The low band’s frequency range was 0.01 to 0.99 Hz, meanwhile the high band’s frequency range was 1 to 1,000 Hz.

A custom made petri dish was created for the purpose of the EIS experiment. A header pin was epoxied on one side of the dish to allow conduction of the electrolyte to the negative terminal of the potentiostat. The petri dish was then filled with 0.9% NaCl solution (standard physiological saline). The wafer was submerged into the solution, the positive end of the potentiostat was connected to the wire of the 10 mm electrode, meanwhile the negative end of the potentiostat was clamped to the header pin on the outside of the petri dish.

PEIS was run using ECLab software on each electrode three times and the results were averaged out. For each successive run, the wafer was rotated 120° to average the distance between the electrode to the negative terminal of the potentiostat. The positive terminal was not moved between each successive run to ensure constant contact resistance between the wire and the positive clamp of the potentiostat. Once "low" band and "high" band measurements were done for the 10 mm Ag/AgCl electrode, the positive end of the potentiostat was moved to the 8.6 mm and so on until we completed the measurements for the wafer.

GEIS was then run on the wafer for a comparison. The experiment was then repeated with 1 more wafer (total of 2 wafers) to ensure wafer-to-wafer variability was averaged out. The same was repeated for the 2 wafers that contained Au electrodes. Finally, both PEIS and GEIS were run on 2 x 3M RedDot electrodes (3M, Inc. - Saint Paul, MN) using the same parameters as above by connecting the clamping the positive terminal of the potentiostat with the button connector of the electrode.

Data Processing:

The raw files from the ECLab software were imported to a text file which was then processed via a spreadsheet. The data from the "low" band and "high" band were combined. The data from run 1, 2, and 3 for each electrode diameter was averaged. This process was repeated for

each of the two wafers both for Ag/AgCl and Au, as well as for the 3M RedDot electrode. We then used Python 3.7.6 to extract the magnitude impedance recorded and create the plots for data comparison. Further, because goal of the study is to understand the effects of electrode diameter for the EGG signal at 0.05 Hz, we extract only the data at 0.05 Hz and construct an exponential model such that the magnitude impedance can be extrapolated for electrodes of any diameter.

Acknowledgments

The authors would like to acknowledge useful discussion about electrode characterization from Prof. Shadi Dayeh and Ritwik Vatsyayan. J.F.K and A.A contributed equally to the work. Further, the authors would like to acknowledge graphic design assistance from Sebastian Podiono. T.P.C acknowledges support from NIH 1 R03 EB031189. This work was performed in part at the San Diego Nanotechnology Infrastructure (SDNI) of UCSD, a member of the National Nanotechnology Coordinated Infrastructure (NNCI), which is supported by the NSF grant ECCS-1542148.

This chapter, in full, is currently being prepared for submission for publication of this material. Jonas F. Kurniawan, Alexis Allegra, Timothy Pham, Andrew K. L. Nguyen, Nathan L. J. Sit, Boris Tjhia, Andrew J. Shin, Todd P. Coleman. The dissertation author was the primary investigator of this material.

References

[1] Kim, D. H., Lu, N., Ma, R., Kim, Y. S., Kim, R. H., Wang, S., ... & Rogers, J. A. (2011). Epidermal electronics. *science*, *333*(6044), 838-843.

[2] Newson, J. J., & Thiagarajan, T. C. (2019). EEG frequency bands in psychiatric disorders: a review of resting state studies. *Frontiers in human neuroscience*, *12*, 521.

[3] Saby, J. N., & Marshall, P. J. (2012). The utility of EEG band power analysis in the study of infancy and early childhood. *Developmental neuropsychology*, *37*(3), 253-273.

[4] Gharibans, A. A., Kim, S., Kunkel, D. C., & Coleman, T. P. (2016). High-resolution electrogastrogram: a novel, noninvasive method for determining gastric slow-wave direction and speed. *IEEE Transactions on Biomedical Engineering*, *64*(4), 807-815.

[5] Gharibans, A. A., Smarr, B. L., Kunkel, D. C., Kriegsfeld, L. J., Mousa, H. M., & Coleman, T. P. (2018). Artifact rejection methodology enables continuous, noninvasive measurement of gastric myoelectric activity in ambulatory subjects. *Scientific reports*, *8*(1), 1-12.

[6] Gharibans, A. A., Coleman, T. P., Mousa, H., & Kunkel, D. C. (2019). Spatial patterns from high-resolution electrogastrography correlate with severity of symptoms in patients with functional dyspepsia and gastroparesis. *Clinical Gastroenterology and Hepatology*, *17*(13), 2668-2677.

[7] Kurniawan, J. F., Tjhia, B., Wu, V. M., Shin, A., Sit, N. L., Pham, T., ... & Coleman, T. P. (2021). An Adhesive-Integrated Stretchable Silver-Silver Chloride Electrode Array for Unobtrusive Monitoring of Gastric Neuromuscular Activity. *Advanced Materials Technologies*, *6*(5), 2001229.

[8] Ganji, M., Tanaka, A., Gilja, V., Halgren, E., & Dayeh, S. A. (2017). Scaling effects on the electrochemical stimulation performance of Au, Pt, and PEDOT: PSS electrocorticography arrays. *Advanced Functional Materials*, *27*(42), 1703019.

[9] Ganji, M., Elthakeb, A. T., Tanaka, A., Gilja, V., Halgren, E., & Dayeh, S. A. (2017). Scaling effects on the electrochemical performance of poly (3, 4-ethylenedioxythiophene (PEDOT), Au, and Pt for electrocorticography recording. *Advanced Functional Materials*, *27*(42), 1703018.

[10] Yu, K. J., Kuzum, D., Hwang, S. W., Kim, B. H., Juul, H., Kim, N. H., ... & Rogers, J. A. (2016). Bioresorbable silicon electronics for transient spatiotemporal mapping of electrical activity from the cerebral cortex. *Nature materials*, *15*(7), 782-791.

[11] Tian, L., Zimmerman, B., Akhtar, A., Yu, K. J., Moore, M., Wu, J., ... & Rogers, J. A. (2019). Large-area MRI-compatible epidermal electronic interfaces for prosthetic control and cognitive monitoring. *Nature biomedical engineering*, *3*(3), 194-205.

[12] Merrill, D. R. (2010). The electrochemistry of charge injection at the electrode/tissue interface. In *Implantable Neural Prostheses 2* (pp. 85-138). Springer, New York, NY.

[13] Hung, A., Goldberg, I. B., & Judy, J. W. (2009). Stimulation electrode materials and electrochemical testing methods. In *Implantable Neural Prostheses 2* (pp. 191-216). Springer, New York, NY.

[14] Tallgren, P., Vanhatalo, S., Kaila, K., & Voipio, J. (2005). Evaluation of commercially available electrodes and gels for recording of slow EEG potentials. *Clinical Neurophysiology*, *116*(4), 799-806.

[15] Albulbul, A. (2016). Evaluating major electrode types for idle biological signal measurements for modern medical technology. *Bioengineering*, *3*(3), 20.

[16] Allegra, A. B., Gharibans, A. A., Schamberg, G. E., Kunkel, D. C., & Coleman, T. P. (2019). Bayesian inverse methods for spatiotemporal characterization of gastric electrical activity from cutaneous multi-electrode recordings. *PloS one*, *14*(10), e0220315.

[17] Zanos, T. P., Silverman, H. A., Levy, T., Tsaava, T., Battinelli, E., Lorraine, P. W., ... & Bouton, C. E. (2018). Identification of cytokine-specific sensory neural signals by decoding murine vagus nerve activity. *Proceedings of the National Academy of Sciences*, *115*(21), E4843-E4852.

[18] Kusayama, T., Wong, J., Liu, X., He, W., Doytchinova, A., Robinson, E. A., ... & Chen, P. S. (2020). Simultaneous noninvasive recording of electrocardiogram and skin sympathetic nerve activity (neuECG). *Nature protocols*, *15*(5), 1853-1877.

[19] Tonog, P., & Lakhkar, A. D. (2019). Normal saline.

[20] Klett, M., Gilbert, J. A., Pupek, K. Z., Trask, S. E., & Abraham, D. P. (2016). Layered oxide, graphite and silicon-graphite electrodes for lithium-ion cells: effect of electrolyte composition and cycling windows. *Journal of The Electrochemical Society*, *164*(1), A6095.

[21] Galloway, J., Syed, A., Kang, W., Kim, J., Cannis, J., Ka, Y., ... & Ryu, S. (2005). Mechanical, thermal, and electrical analysis of a compliant interconnect. *IEEE Transactions on Components and Packaging Technologies*, *28*(2), 297-302.

Figures

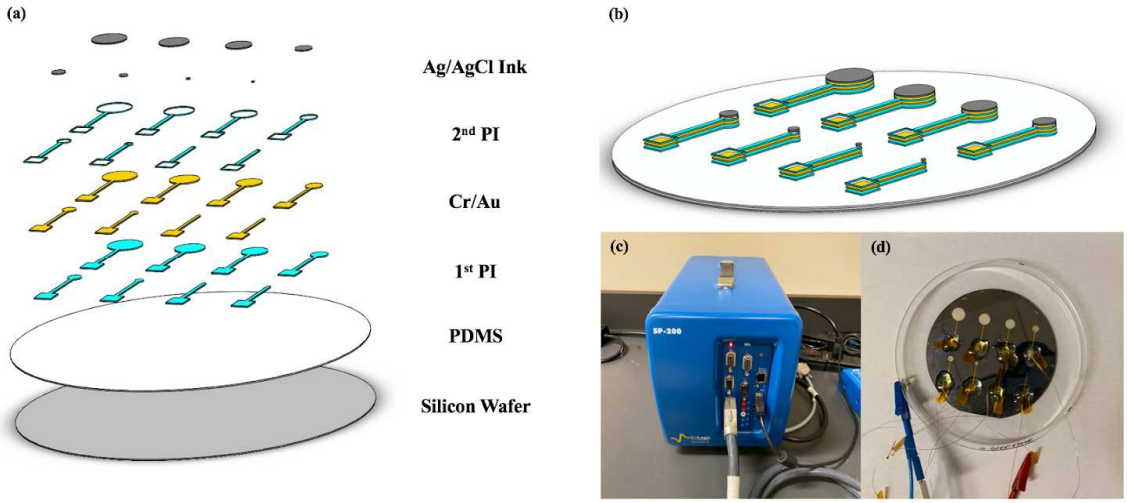

Figure 2.1. (a) An exploded view of the device cross section for the EIS experiment (1 - 10 mm sensor diameter). For the Au electrodes, the Ag/AgCl ink was not screen printed post cleanroom process. **(b)** A schematic view of the wafer used for the EIS experiment. The bonding pads and the interconnects are the same size for each electrode. **(c)** The Biologic SP-200 potentiostat used to run the EIS experiment. **(d)** The experimental setup for the EIS experiment, each individual pad was soldered using a thin wire and epoxied to insulate the pad. In the two electrode system, the red (+) terminal was attached to each electrode of interest and the blue (-) terminal was attached to the petri dish via a pin header. The dish was filled up to the fill line with 0.9% NaCl solution, the fill line was predetermined before the experiment to ensure the full immersion of the wafer.

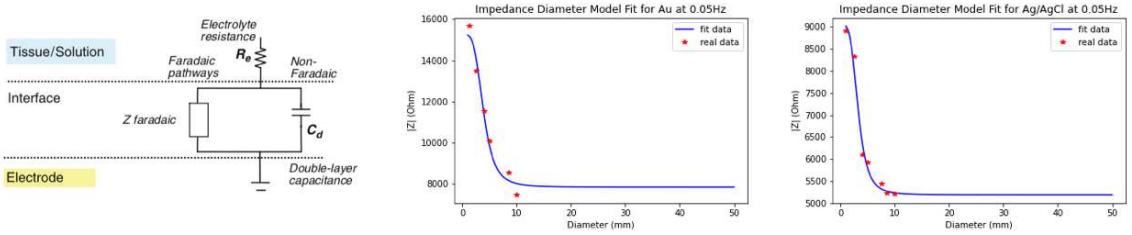

Figure 2.2. (Left) Simple electrode/electrolyte model to describe the behavior of the electrode. **(Middle)** A plot of |Z| against electrode diameter in the study for Au flex electrodes at a 0.05 Hz frequency. Here, the results of each wafer were plotted and a simple Randles circuit fit was made. **(Right)** A plot of |Z| against electrode diameter in the study for Au flex electrodes at a 0.05 Hz frequency. Here, the results of each wafer were plotted and a simple Randles circuit fit was made. Generally, the values of Ag/AgCl were lower than that of Au for the same electrode diameter.

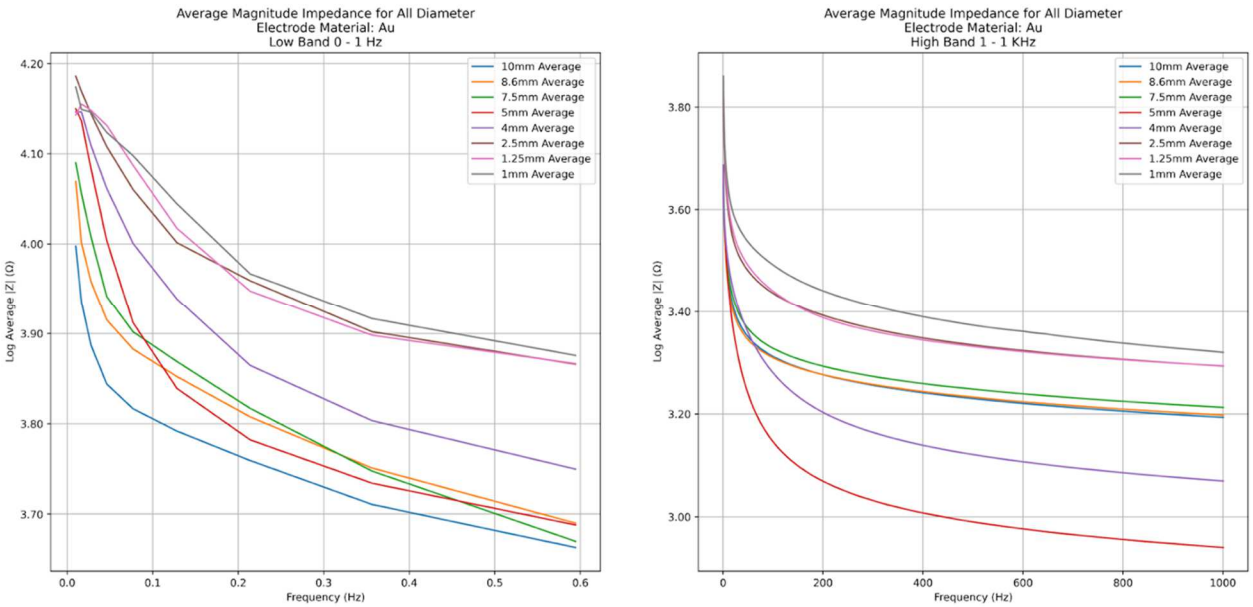

Figure 2.3. (Left) A plot of the magnitude impedance vs frequency for the low band. **(Right)** A plot of magnitude impedance vs frequency for the high band of Au flexible electrodes. Low band is defined as 0 - 1 Hz and high band is 1 - 1,000 Hz.

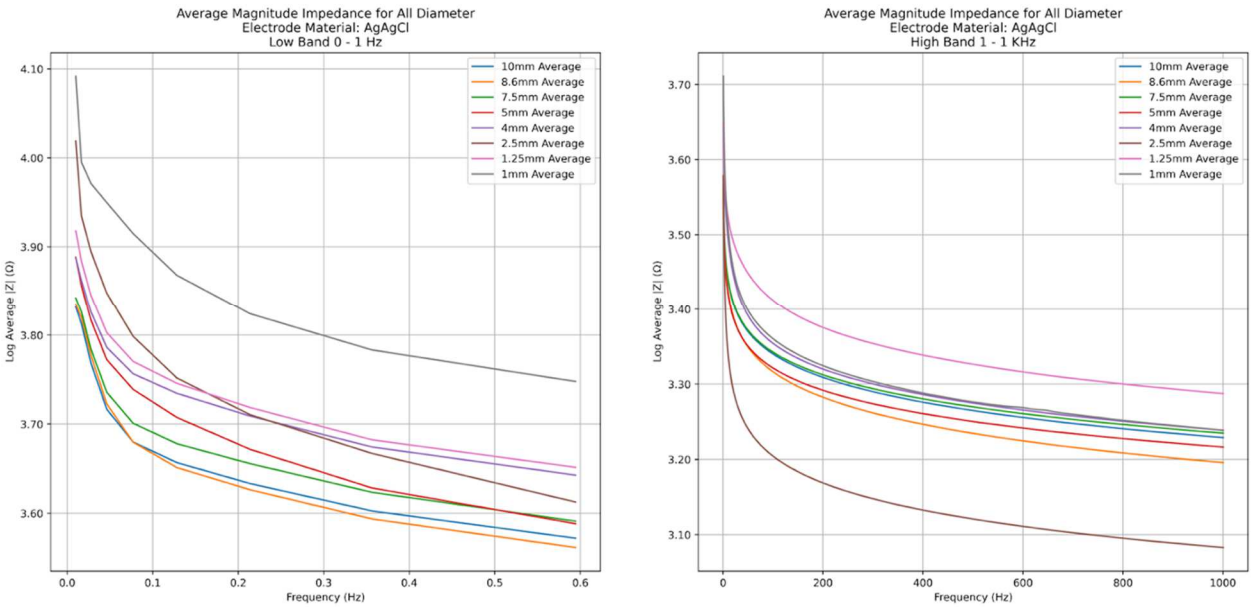

Figure 2.4. (Left) A plot of the magnitude impedance vs frequency for the low band. **(Right)** A plot of magnitude impedance vs frequency for the high band of Ag/AgCl flexible electrodes. Low band is defined as 0 - 1 Hz and high band is 1 - 1,000 Hz.

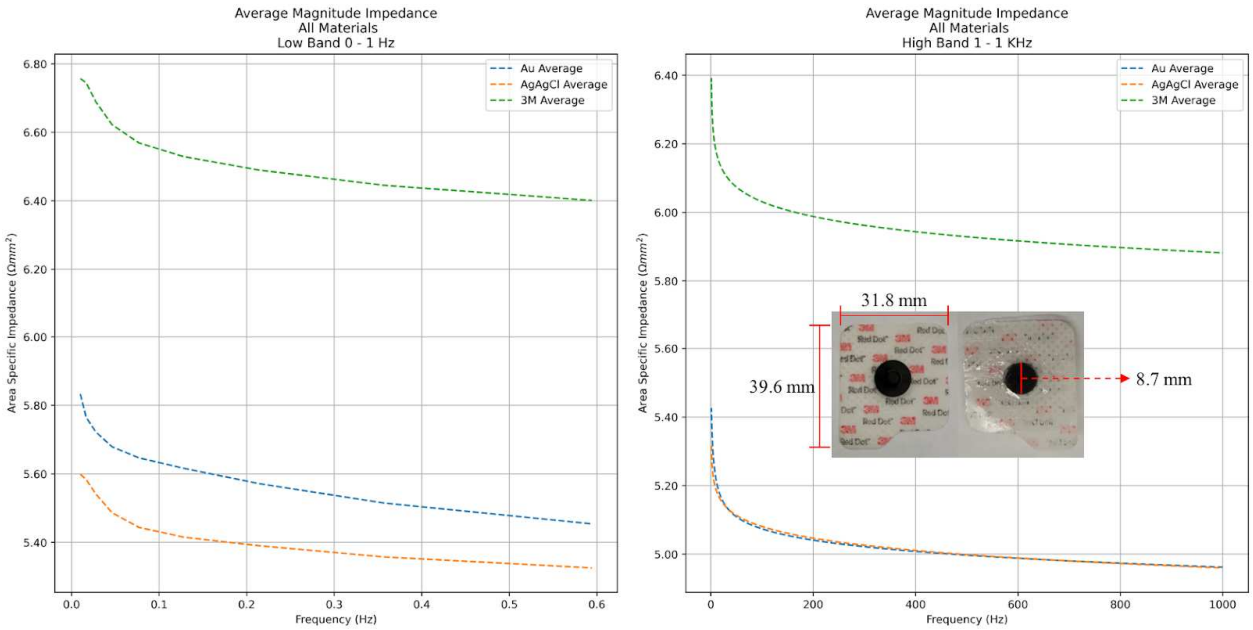

Figure 2.5. Graphs of area specific impedance (ASI) vs frequency at the low band and high band. The area specific impedance was plotted using a log scale and frequency was done in linear scale. For comparison purposes across different electrode types, a specific electrode diameter of 8.6 mm was chosen as it is the diameter of a standard 3M RedDot electrode. On the low band plot (left), we can see that the ASI of 3M RedDot is the lowest, followed by Ag/AgCl, and finally Au being the highest. Similarly, on the high band plot (right), we can see that the ASI of 3M RedDot is also the lowest, followed by Ag/AgCl and Au which have similar values across multiple frequencies.

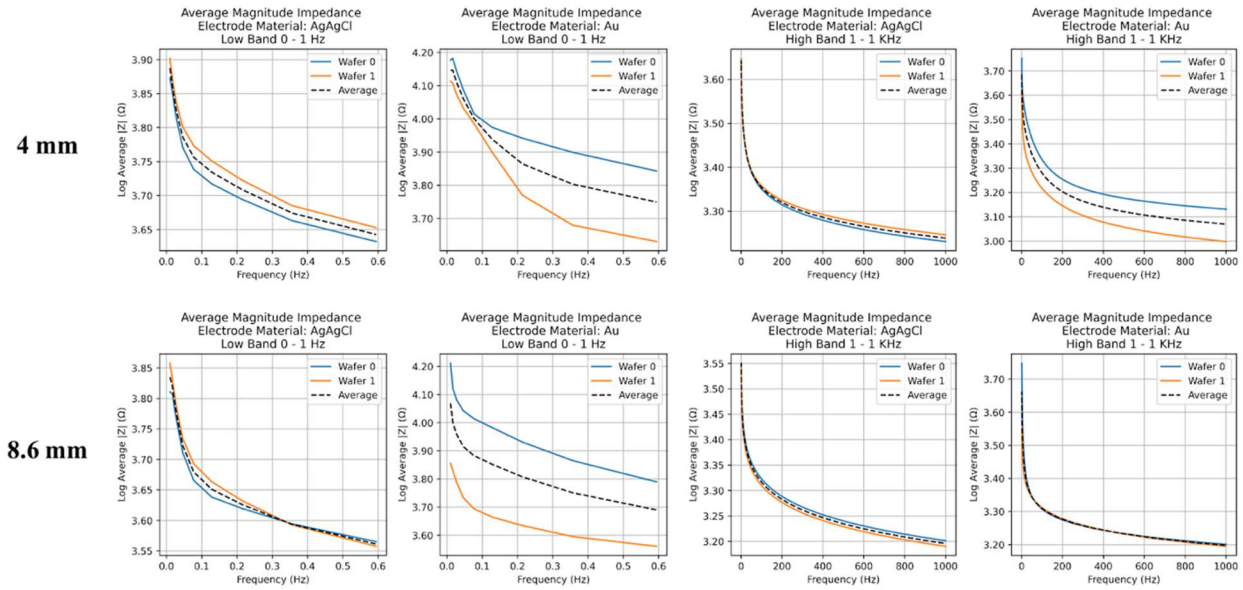

Figure 2.6. Average magnitude impedance for both Au and Ag/AgCl flexible electrodes. These two plots indicate wafer-to-wafer variability on impedance for both materials. For the purpose of comparison, we chose 4 mm and 8.6 mm as the electrode diameters. It could be seen from all the figures that generally Ag/AgCl had less variability in magnitude impedance compared to Au, especially in the low band.

Chapter 3. Non-Invasive Measurement of Cervical Neuronal Activities via an Adhesive-Integrated Flexible Surface Electrodes

Abstract

Here, an adhesive-integrated flexible electrode array for non-invasive monitoring of neuronal activities is introduced. This peel-and-stick device pioneered recording of neuronal activities in human subject. Previously, electrode cuffs have been used in preclinical models to measure its neuronal activity. Utilizing silver-silver chloride as material of choice, combined with HackEEG biopotential board and custom GUI, we are able to reach a high signal to noise ratio over duration of the recordings. As a stress to the autonomnic nervsous sytem, we employed the Cold-pressor test to demonstrate the capability of our surface electrodes in detecting neuron spikes. Custom algorithm spike sorting further enabled us to classify neural activity. This work paves a future path for ambulatory non-invasive recording of neuronal activity which may provide an early signal that indicates a change autonomic nervous system activity.

Keywords: surface electrodes, vagus nerve, dermal sympathetic nerve, flexible electronics, wireless monitoring.

Introduction

The autonomic nervous system (ANS) links the central nervous system (CNS; brain and spinal cord) with the peripheral organ systems that include: integumentary (sweat glands), circulatory (heart, blood vessels), digestive (gastrointestinal tract glands and sphincters,kidney, liver, salivary glands), endocrine (adrenal glands), reproductive (uterus, genitals), respiratory (bronchiole smooth muscles), urinary (sphincters), and visual (pupil dilator and ciliary muscles) [1-3]. The autonomic nervous system colloquially is divided in to two main divisions: the sympathetic nervous system and parasympathetic nervous system that simultaneously work together in concert to carefully control peripheral organ systems [4, 5]. A large body of empirical evidence suggests that autonomic nervous system imbalance is associated with various pathological conditions that can include and heterogeneous disease states that include: diabetic autonomic neuropathy, hyperhidrosis, orthostatic intolerance/postural tachycardia syndrome, pure autonomic failure, and vasovagal syncope.

At the human cervical neck multiple components of the autonomic nervous system are in close approximation. This includes the major parasympathetic neuronal output transmitted by the Vagus nerve, which communicates directly to the visual, heart, respiratory and the digestive systems. A major sympathetic neuronal output transmitted by the superior cervical ganglion is located approximately 1-2 cm deep to the vagus nerve. Sympathetic fibers have been observed in vagus nerve fascicles, suggesting overlapping sympathetic and parasympathetic signaling is inherent in vagus nerve transmission [6]. The superior cervical ganglion along with thoracic sympathetic output directly to the integumentary, visual, circulatory, (heart and blood vessels), respiratory, and digestive organ systems. Given the immense peripheral organ system control generated from cervical autonomic neuronal structures found within the superficial cervical neck

[7] there is an unmet need to decode and further understand these signals in health and disease. Prior preclinical[8] work recorded resting microelectrode vagus nerve action potentials during a stress model such as Lipopolysaccharide, or inflammatory cytokine injection [9, 10]. One recent human study measured microelectrode human vagus nerve action potentials that showed synchronization with the respiratory cycle[11] that support prior preclinical porcine work[12, 13]. Preclinical lamb superior cervical ganglion activity was measured with cuff electrode at rest with hypertensive stress tests, i.e., injection of adrenaline [14]. To date human cervical vagus nerve superior cervical ganglion recording do not exist with any stress model, likely due to the risk associated with acute and chronic surgical cuff electrode implantation. To address this knowledge gap we developed a noninvasive, adhesive-integrated and skin conformal silver-silver chloride electrode array was designed and positioned over the human left superior anterior cervical area overlying multiple neural structures (i.e. including the vagus nerve and its branches, sympathetic chain and its branches, the hypoglossal and glossopharyngeal nerves as well as muscle and dermal sympathetic nerves) during a commonly employed stress test, i.e., the cold pressor stress test (CPT). The cold pressor test (CPT) is performed by immersing the hand into an ice water container, usually for one minute. It triggers the subject's vascular sympathetic activation and increases blood pressure [15, 16]. It also increases vagal tone by activating dorsal medulla that are part of the vagus nerve pathways [17, 18]. The effect of CPT on heart rate is variable, being either an increase or remaining unchanged [19].

We hypothesized that the recorded signals from the electrode array are capable of measuring 1) superficial neural structures, i.e. dermal sympathetic nerve. 2) deep neural structures, i.e. vagus nerve and superior sympathetic ganglia.

Results

Our state of the art surface electrode array can adhesively, flexibly and non-invasively attach to the subject's cervical area. And all our subjects can freely move their necks without distorting the adhesiveness and robustness of our surface array. Due to the low impedance between the electrodes and skin, the powerline noise and its harmonics are also minimized in our measurement.

In post-processing, all five channel signals for each CPT measurement were run through the spike sorting algorithm we proposed above. The heart rate change was also estimated from the ECG signal by calculating the intervals between each consecutive QRS peaks. The Spike sorting analysis result for the CPT from one of our subjects was presented in Figure 3. In all of its subplots, the green vertical line is when the CPT started and the subject immersed his right hand into the ice bucket while the red vertical line is when the CPT stopped. The spike sorting analysis from the top channel of the electrode array at the skin surface above the nodose ganglion is shown in **Figure 3. 3**a. The heart rate is plotted in magenta using the right y-axis. We can see there is an increasing neuronal activity and heart rate during the CPT compared with the baseline activity. To get an accurate estimate of the change of neuronal activity, the data was run through the spike sorting analysis and the peak of each detected spike was also marked in dots with different colors, representing the different clusters they belong to. **Figure 3.3**b shows four selected clustered spikes information from the top channel of the electrode. The left panel is the waveform average of the clustered spikes showing waveform shape. The right panel displays the amplitude (peak to peak difference) and the firing rate of the cluster over the duration of the experiment. The amplitude is plotted on the top half of the plot using the right y-axis while the firing rate is plotted in histogram at the bottom using the left y-axis. We can see that in cluster 2 there is a clear increasing firing rate

during CPT compared with its baseline activity. Note that cluster 1 is the outlier cluster, which aggregates all spikes that have low density in the 2D projection by the t-SNE and the DBSCAN algorithm.

The spike sorting analysis for the electrode at the skin area of the carotid artery from the same CPT experiment is shown in **Figure 3.3**c. As the top electrode, there is an increasing neuronal activity observed during the CPT period. **Figure 3.4**c shows four selected clustered spikes information from the spike sorting result. There are multiple clusters (cluster 4, 5, 7) shown increasing firing rate during CPT compared with baseline activity. Again, cluster 1 represents the outlier cluster.

Statistical analysis was also performed to identify responsive clusters, i.e., which clustered group has significant firing during CPT comparing with baseline activity. First, the mean and the standard deviation of the firing frequency for each cluster at baseline was estimated. Then, for a cluster to be considered as a responsive cluster, its average firing frequency during CPT has to be 3 standard deviations more than its baseline activity for at least 40% of stress challenge. For the electrodes at both the nodose ganglion and the carotid artery, 5 different clusters were found as responsive clusters independently (**Figure 3.4**). And these responsive clusters gradually return to baseline level in a minute after CPT.

Discussion

In this work, we present a flexible, adhesive-integrated electrode array for non-invasive monitoring neural activities at the cervical area. The peel-and-stick device substitutes the invasive and cumbersome needle electrode. Because of the self-adhesive and non-invasive nature of the electrode array, it is feasible to perform recordings over a prolonged period of time. Overlying the

electrode array at the left superior anterior cervical area, we measure multiple neural structures simultaneously including the vagus nerve and its branches, sympathetic chain and its branches, the hypoglossal and glossopharyngeal nerves as well as muscle and dermal sympathetic nerves.

The HackEEG system integrates the ADS1299 chip which can sample 8 channels data at 16k sampling rate with 24bit ADC resolution. The small enclosure nature of the HackEEG system enables us to attach the system on subject body with a belt at subject's chest. Considering the neural activity of our interest is no more than 1000 Hz, we picked sampling rate at 8k Hz for efficiency purposes. Customized GUI could plot recordings for us in real time to monitor responses and abnormalities during measurement.

We have chosen silver/silver chloride (Ag/AgCl) to be the material for the sensor due to three main reasons, namely high signal-to-noise ratio, lower skin-to-electrode impedance compared to Au electrode, and the non-polarizable nature of Ag/AgCl. Ag/AgCl electrodes allow Cl^- ions to partake in free charge exchange which prevents charge buildup [24-26].

Ag/AgCl was chosen to be the material for the sensor layer due to high signal-to-noise ratio, lower skin-to-electrode impedance, and the non-polarizable nature of Ag/AgCl electrodes which allows Cl^- ion to take part in free charge exchange which prevents charge buildup [24-26]. Previously, it was demonstrated that flexible electrodes which utilized Ag/AgCl was successful in measuring other biopotential signals such as electrogastrogram (EGG) [24]. Thus, Ag/AgCl was seen as an appropriate material for our flexible neuronal electrodes due to its superior recording quality compared to gold flexible electrode [24-26]. Further, the combination of ambulatory monitoring via HackEEG boppotential board and custom GUI allowed a convenient recording of the subject's neuronal activities.

The most direct measured signal is the dermal sympathetic nerves, also known as skin sympathetic nerve activity. To the best of knowledge, the only proved technology for measuring skin sympathetic nerve activity is by extracting high frequency components from ECG measurement[23]. In our measurement, we performed the same CPT experiment, we also saw a clear increased response during CPT and the response gradually returned to baseline level after CPT experiment. As our electrode array was placed along with the vagus trace from the nodose ganglion to the carotid artery, we simultaneously measure the deeper structure from the parasympathetic nerve. Electromyography (EMG) signal may also be captured by our electrodes from the cricothyroid muscle group. However, as our subjects were told to stay still, keep quiet and avoid swallowing during experiment, the EMG activity would only be recorded at the beginning and end of the CPT from the arm movements.

By conducting the spike sorting analysis, we decomposed spike waveforms detected from each measurement into multiple clusters. The waveform had closer spatial distance at low dimension representation were clustered as the same group. Each cluster represented neural activity from different neural structure under the surface electrodes. We found that at each measurement position, multiple neural groups had significant increasing response compared with baseline during CPT, and these groups' activities back to baseline after CPT experiment.

In this work, we presented a flexible and adhesive-integrated electrode surface array that can noninvasively measure multiple neural structures at the cervical area including dermal sympathetic nerve, vagus nerve, hypoglossal and glossopharyngeal nerves as well as cricothyroid muscle group. With the advanced spike sorting algorithm, we decomposed measurement into different neural activity clusters and showed that multiple of these neural structures have increased activities under stress challenge.

Experimental Section/Methods

Electrodes Array Fabrication:

A 4" silicon wafer was cleaned with acetone, IPA, DI water, IPA followed by drying with N_2 gun. The wafer then underwent a dehydration bake at 180°C on a contact hotplate. Subsequently, polydimethylsiloxane (PDMS) which would act as a weakly adhering substrate was spun coated at 4000 rpm. Polyimide (HD Microsystems, Inc. - Parlin, NJ) was then spun coated at 4000 rpm followed by a soft bake at 110°C for 1 min and at 150°C for 5 min on a contact hotplate. A full hard bake in N_2 rich environment oven at 300°C then followed. Metalization was performed on an electron beam evaporator (Temescal BJD 1800 E-Beam Evaporator - Livermore, CA) to yield a 10 nm chrome and a 500 nm gold layer. Sensors (5 mm diameter) and interconnects (500 um width) were then defined via standard lithographic procedures. Another layer of polyimide was then applied using the same parameters as above. Photolithography and reactive ion etching (RIE) with O_2 plasma followed to define the bottom and top polyimide layer which acted as insulator layers.

Post cleanroom processing, a silver/silver chloride ink (Creative Materials, Inc. - Ayer, MA) was screen printed onto the active sensor areas via a standard stainless steel stencil (Metal Etch Services, Inc. - San Marcos, CA). A custom zero insertion force (ZIF) connector was then interfaced with the electrode array using anisotropic tape which facilitated bonding (3M, Inc. - Saint Paul, MN) by applying heat and pressure on the bonding sites. Water soluble tape (3M, Inc. - Saint Paul, MN) was then used to transfer print the device from the silicon wafer to a flexible silicone substrate made on a 5" petri dish that was spun coated at 3000 rpm with Ecoflex (Smooth On, Inc. - Macungie, PA) which acted as a backbone silicone and Silbione RT Gel (Elkem, Inc. - Brunswick, NJ) which acted as an adhesive silicone. The silicone substrate and the device were then peeled off and transferred to a thin sheet of PET (Grafix - Maple Heights, OH) which acted

as a backing that eased handling of the device. The silicone bilayer was then cut into a rectangular shape which yielded the final sensor array as shown in **Figure 4.1**d.

Participants:

Recordings were performed on 10 healthy subjects (N=2 females and N=8 males, age: 21.8 ± 2.1 years)

Electrode Placement:

Conductive gel was applied to the electrode surface using a syringe to help with the conductivity. The device was then applied to the neck with the top electrode approximately at the skin above the nodose ganglion and the bottom electrode at the skin above the carotid artery. Once attached, the PET backing was peeled off (Figure 2a). The ZIF connector was attached to a breakout board (Adafruit Industries, Inc - New York, NY) which then connected via cables to a biopotential data acquisition board (HackEEG) along with ground and reference electrodes (3M Red Dot, 3M, Inc - Saint Paul, MN). Electrocardiography (ECG) was also monitored by the 3M electrodes that were placed on the right upper chest and left bottom rib.

Data Collection:

Subjects were recruited at University of California San Diego (UCSD). Before the device application, the electrode placement area was abraded by the abrasive pads (BIOPAC system Inc, Goleta, CA, USA) and prepped using alcohol pads to exfoliate dead skin. A ground electrode was placed on the left forearm of the subject and an additional reference electrode was placed ipsilaterally above the flexible sensor array at the mastoid. Data was collected and streamed to the open source HackEEG data acquisition system (Starcat LLC, Seattle WA, USA). HackEEG is a high-performance, open-source Arduino Due shield for the Texas Instrument ADS1299 system on

chip. It can digitize 8-channel bio signals simultaneously at 24 bit analog-digital conversion resolution at 8000 samples per second with user-selectable gain from 1 to 24. The HackEEG system is enclosed in a 3D printed box with dimension 13cm × 7cm × 5cm, (Figure 2b).

Data Processing:

A customized graphic user interface (GUI) installed on a Linux terminal was written in python to monitor physiological signals in real time. In post processing, the cervical signal was filtered by a 20-1,000 Hz zero-phase bandpass filter. Powerline noise and harmonics were also removed by notch filters. In each cervical neural recording, a spike sorting algorithm was carried out to differentiate detected spikes into different clusters. First, spike detection is performed by setting a threshold as:

$$\text{Thr} = 3\sigma, \text{ with } \sigma = \text{median}\left(|x|/0.6745\right),$$

where x is the bandpass filtered signal[20]. For each detected spike, the waveform, 80 samples (10ms) were saved as the candidate waveform template, aligned to their maximum at data point 30 (3.75ms). Dimensionality reduction for feature extraction was run through the T-distributed stochastic neighbor embedding (t-SNE) on all candidate spikes to enable a representative visualization[21]. The low dimension projection was then run through the unsupervised classification algorithm, the density-based spatial clustering of application with noise (DBSCAN) [22] to cluster spikes into groups. The clustered neural groups were characterized by different firing rate and amplitude behaviors. The firing rate was counted as the number of neural group activity per second and the amplitude was derived by calculating the peak to peak difference of each detected waveform. (**Figure 3.2**c)

Human Experiment:

Data collection was done as part of an ongoing study at the University of California San Diego, whose institutional review board provided ethical approval (IRB # 171154).

Acknowledgments

The authors would like to acknowledge graphic design assistance from Sebastian Podiono. I.L acknowledges support from BARDA Contract #75A50119C00038. Y.B and J.F.K contributed equally to this work. This work was performed in part at the San Diego Nanotechnology Infrastructure (SDNI) of UCSD, a member of the National Nanotechnology Coordinated Infrastructure (NNCI), which is supported by the NSF grant ECCS-1542148.

This chapter, in full, is currently being prepared for submission for publication of this material. Yifeng Bu, Jonas F. Kurniawan, Andrew K. L. Nguyen, Brandon Ho, Nathan L. J. Sit, Timothy Pham, Vincent M. Wu, Boris Tjhia, Andrew J. Shin, Todd P. Coleman, Imanuel Lerman. The dissertation author was the primary investigator of this material.

References

[1] McCorry, L. K. (2007). Physiology of the autonomic nervous system. *American journal of pharmaceutical education*, *71*(4).

[2] Zygmunt, A., & Stanczyk, J. (2010). Methods of evaluation of autonomic nervous system function. *Archives of medical science: AMS*, *6*(1), 11.

[3] Marques, A. H., Silverman, M. N., & Sternberg, E. M. (2010). Evaluation of stress systems by applying noninvasive methodologies: measurements of neuroimmune biomarkers in the sweat, heart rate variability and salivary cortisol. *Neuroimmunomodulation*, *17*(3), 205-208.

[4] Jänig, W., & McLachlan, E. M. (1992). Characteristics of function-specific pathways in the sympathetic nervous system. *Trends in neurosciences*, *15*(12), 475-481.

[5] Levy, M. N., Koeppen, B. M., & Stanton, B. A. (2005). *Berne & Levy Principles of Physiology E-Book*. Elsevier Health Sciences.

[6] Seki, A., Green, H. R., Lee, T. D., Hong, L., Tan, J., Vinters, H. V., ... & Fishbein, M. C. (2014). Sympathetic nerve fibers in human cervical and thoracic vagus nerves. *Heart rhythm*, *11*(8), 1411-1417.

[7] Olshansky, B., Sabbah, H. N., Hauptman, P. J., & Colucci, W. S. (2008). Parasympathetic nervous system and heart failure: pathophysiology and potential implications for therapy. *Circulation*, *118*(8), 863-871.

[8] Zanos, T. P., Silverman, H. A., Levy, T., Tsaava, T., Battinelli, E., Lorraine, P. W., ... & Bouton, C. E. (2018). Identification of cytokine-specific sensory neural signals by decoding murine vagus nerve activity. *Proceedings of the National Academy of Sciences*, *115*(21), E4843-E4852.

[9] Zanos, T., Silverman, H., Levy, T., Tsaava, T., Battinelli, E., Lorraine, P., ... & Tracey, K. J. (2018). Identification of cytokine-specific sensory neural signals in murine vagus nerve activity recordings.

[10] Marmerstein, J. T., McCallum, G. A., & Durand, D. M. (2021). Direct measurement of vagal tone in rats does not show correlation to HRV. *Scientific reports*, *11*(1), 1-12.

[11] Ottaviani, M. M., Wright, L., Dawood, T., & Macefield, V. G. (2020). In vivo recordings from the human vagus nerve using ultrasound-guided microneurography. *The Journal of Physiology*, *598*(17), 3569-3576.

[12] Sevcencu, C., Nielsen, T. N., Kjærgaard, B., & Struijk, J. J. (2018). A respiratory marker derived from left vagus nerve signals recorded with implantable cuff electrodes. *Neuromodulation: Technology at the Neural Interface*, *21*(3), 269-275.

[13] Vallone, F., Ottaviani, M. M., Dedola, F., Cutrone, A., Romeni, S., Panarese, A. M., ... & Micera, S. (2021). Simultaneous decoding of cardiovascular and respiratory functional changes from pig intraneural vagus nerve signals. *Journal of Neural Engineering*.

[14] Cassaglia, P. A., Griffiths, R. I., & Walker, A. M. (2008). Sympathetic nerve activity in the superior cervical ganglia increases in response to imposed increases in arterial pressure. *American Journal of Physiology-Regulatory, Integrative and Comparative Physiology*, *294*(4), R1255-R1261.

[15] Seals, D. R. (1990). Sympathetic activation during the cold pressor test: influence of stimulus area. *Clinical physiology*, *10*(2), 123-129.

[16] Victor, R. G., Leimbach Jr, W. N., Seals, D. R., Wallin, B. G., & Mark, A. L. (1987). Effects of the cold pressor test on muscle sympathetic nerve activity in humans. *Hypertension*, *9*(5), 429-436.

[17] Ghiasi, S., Greco, A., Barbieri, R., Scilingo, E. P., & Valenza, G. (2020). Assessing autonomic function from electrodermal activity and heart rate variability during cold-pressor test and emotional challenge. *Scientific reports*, *10*(1), 1-13.

[18] Hendriks-Balk, M. C., Megdiche, F., Pezzi, L., Reynaud, O., Da Costa, S., Bueti, D., ... & Wuerzner, G. (2020). Brainstem Correlates of a Cold Pressor Test Measured by Ultra-High Field fMRI. *Frontiers in neuroscience*, *14*, 39.

[19] Elias, S. O., & Ajayi, R. E. (2019). Effect of sympathetic autonomic stress from the cold pressor test on left ventricular function in young healthy adults. *Physiological reports*, *7*(2), e13985.

[20] Quiroga, R. Q., Nadasdy, Z., & Ben-Shaul, Y. (2004). Unsupervised spike detection and sorting with wavelets and superparamagnetic clustering. *Neural computation*, *16*(8), 1661-1687.

[21] Van Der Maaten, L. (2014). Accelerating t-SNE using tree-based algorithms. *The Journal of Machine Learning Research*, *15*(1), 3221-3245.

[22] Ester, M., Kriegel, H. P., Sander, J., & Xu, X. (1996, August). A density-based algorithm for discovering clusters in large spatial databases with noise. In *kdd* (Vol. 96, No. 34, pp. 226-231).

[23] Kusayama, T., Wong, J., Liu, X., He, W., Doytchinova, A., Robinson, E. A., ... & Chen, P. S. (2020). Simultaneous noninvasive recording of electrocardiogram and skin sympathetic nerve activity (neuECG). *Nature protocols*, *15*(5), 1853-1877.

[24] Kurniawan, J. F., Tjhia, B., Wu, V. M., Shin, A., Sit, N. L., Pham, T., ... & Coleman, T. P. (2021). An Adhesive-Integrated Stretchable Silver-Silver Chloride Electrode Array for Unobtrusive Monitoring of Gastric Neuromuscular Activity. *Advanced Materials Technologies*, *6*(5), 2001229.

[25] Tallgren, P., Vanhatalo, S., Kaila, K., & Voipio, J. (2005). Evaluation of commercially available electrodes and gels for recording of slow EEG potentials. *Clinical Neurophysiology*, *116*(4), 799-806.

[26] Albulbul, A. (2016). Evaluating major electrode types for idle biological signal measurements for modern medical technology. *Bioengineering*, *3*(3), 20.

Figures

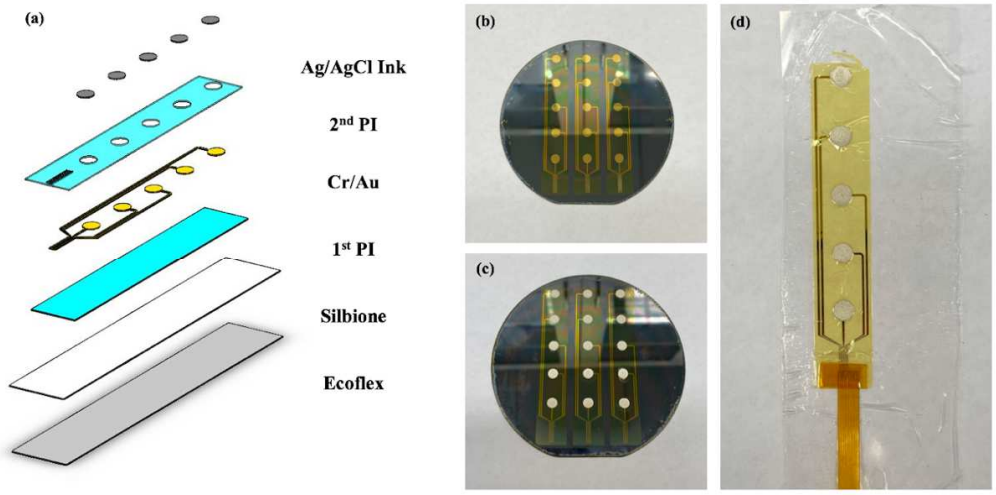

Figure 3.1. (a) Device cross section (5 mm sensor diameter and 500 um interconnect width). **(b)** Cleanroom post-processed wafer ready to be printed with Ag/AgCl ink. **(c)** Ag/AgCl ink screen-printed wafer on the active electrodes region. **(d)** Device transfer-printed into a self-adhering flexible silicone substrate (Ecoflex/Silbione) on PET backing via water soluble tape.

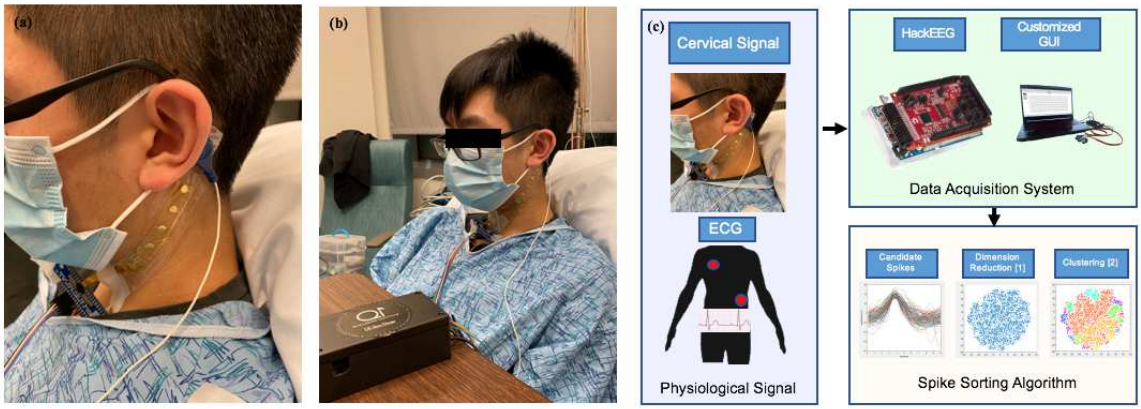

Figure 3.2. (a) The device was attached to the subject with the top electrode in the array attached to the approximate location of the nodose ganglion, further the 3M RedDot electrode was used as a reference electrode. **(b)** The setup used during data collection which involved the flexible multi electrodes attached to a breakout board, a wireless biopotential board (HackEEG), and 3M RedDot ground and reference electrodes. **(c)** A schematic of the experiment workflow. This included the type of signal collected during the experiment, the data acquisition system, as well as post processing algorithms utilized.

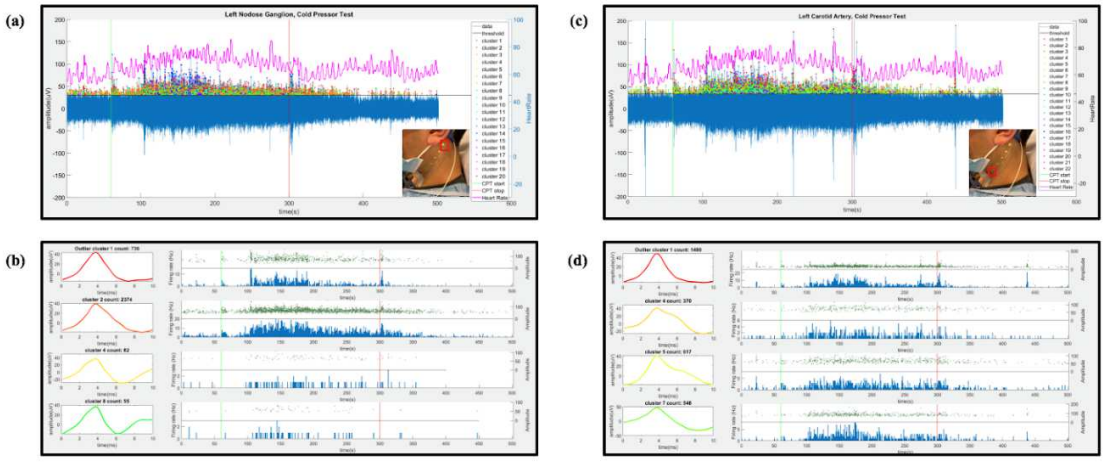

Figure 3.3. The spike sorting analysis for the CPT. The green vertical line is when the CPT started and the subject immersed his or her right hand into the ice bucket while the red vertical line is when the CPT stopped. **(a)** The spike sorting analysis from the top channel of the electrode array at the skin surface above the nodose ganglion. The dots mark the peak of all detected spikes, and their color represents the cluster that each spike belongs to. The heart rate is plotted in magenta using the right y-axis. **(b)** Four selected clustered spikes information from the top channel of the electrode. On the left panel is the waveform average of the clustered spikes showing waveform shape. The right panel displays the amplitude (peak to peak difference) and firing rate of a cluster over the duration of the experiment. For the economy of space, the amplitude is plotted on the top half of the plot using the right y-axis while the firing rate is plotted in histogram at the bottom using the left y-axis. **(c)** The spike sorting analysis from the bottom channel of the electrode array at the skin surface above the carotid artery. **(d)** Four selected clustered spikes information from the bottom channel of the electrode.

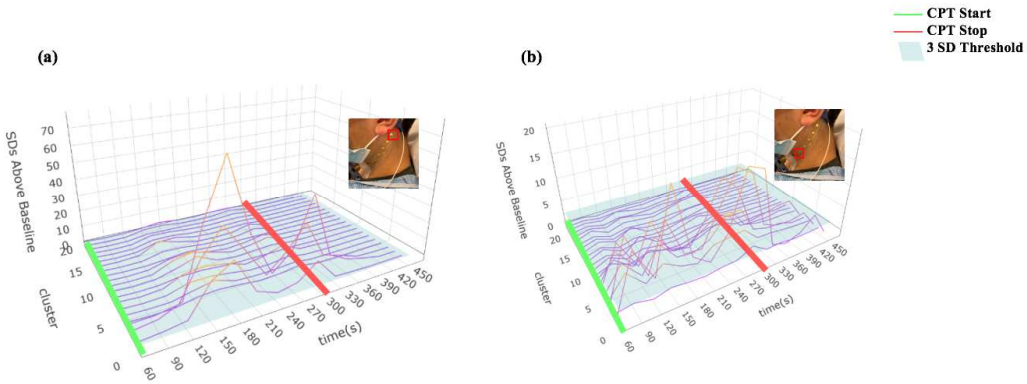

Figure 3.4. (a) Statistical analysis for responsive clusters from the clusters at the upper nodose ganglion measurement. **(b)** Statistical analysis for responsive clusters from the clusters at the bottom carotid artery measurement. CPT start time is denoted by the green line and the CPT stop time is denoted by the red line. There were several clusters that were responsive as shown by the orange lines in the two figures.

Chapter 4. Non-Invasive Multi-Channel Urodyamics (NI Multi-Channel UDS) System is Sensitive and Reliable to Detect Inter-Subject Consistency of Electrical Signals from Human Urinary Bladder

Abstract

We developed a high-resolution and non-invasive multi-channel urodynamic (NI multi-channel UDS) system combined with novel waveform analysis to provide a signature pattern in electrical signals from the urinary bladder. In this study, we utilized a flexible non-invasive electromyogram (EMG) system and a customized board to collect a full set of signals of small electrical currents generated by muscle fibers from the lower abdomen of human subjects. Then the innovation of this study is to suggest a designed set of coding to eliminate noise signals from adjacent organs and sort out specific signals of small electrical currents generated by smooth muscle fibers of the urinary bladder of human subjects.

Keywords: non-invasive (NI) multi-channel urodynamic study (UDS), electrical signal from urinary bladder, voluntary voiding, flexible electronics.

Introduction

The two major functions of the urinary bladder are storage and emptying of urine which requires the coordinated activities of the autonomic and somatic nervous systems, bladder and urethral smooth muscle, bladder mucosal layer and stroma, and the external urethral sphincter. Diseases and injuries that cause alterations anywhere along the neural pathways that control bladder and sphincter function can result in neurogenic lower urinary tract dysfunction or neurogenic bladder (NGB). The manifestations of NGB can vary widely depending on the neurologic deficit. These manifestations can vary from patient to patient. As such, evaluation with conventional multi-channel urodynamic studies (UDS) is often necessary to diagnose the type of bladder dysfunction and to direct therapy [1].

Even in bladders not affected by neurologic injury, additional factors including genetics, dietary habits, metabolic disease and aging can cause changes in bladder activity [2,3,4,5,6]. One of the most common conditions that results from these changes is overactive bladder (OAB) [7]. Patients with OAB usually present with subjective complaints of urgency, frequency, nocturia, and urgency incontinence. From a societal perspective, OAB-associated healthcare costs in 2015 were $76.2 billion dollars [7]. Neurogenic bladder and OAB affect approximately 267,000 and 33 million Americans, respectively. Their impacts on quality of life span various domains and may include urinary tract infections, urinary stones, pain and ultimately renal deterioration. Additionally, bladder dysfunction can affect psychological well-being, social embarrassment and fear of leaving the house, decreased physical exertion, and disturbed sleep. Despite clear guidelines on its management, OAB is challenging to manage effectively. Patient compliance remains a significant challenge, with data suggesting that 92% of OAB patients discontinue their medication within 2 years [7]. A small percentage of patients proceed to third-line therapies, and those who

do are likely to be older than 50 years old, have urinary incontinence, and report symptoms for greater than 4 years. In order to categorize severity of OAB, providers often utilize subjective characterization of symptoms, voiding diaries, patient-reported voided volumes, and non-invasive tests, such as a residual urine volume monitoring and uroflowmetry, to guide treatment. Often, conventional UDS can be used to characterize bladder function and guide treatment planning. However, UDS is often implemented in a delayed manner in the management of overactive bladder because of the invasive nature of the study. There is an unmet need for an early diagnostic test that can effectively characterize bladder function without the invasiveness of conventional UDS.

Conventional multi-channel UDS can be burdensome due to (1) the need for catheter insertion into the bladder and rectum/vagina for recording pressures, (2) limited availability of UDS equipment, which often results in delay in performing the study by several weeks, (3) need for trained clinical staff being present in the study, , which can increase patient anxiety and affect the results, and (4) logistical and time constraints [8,9,10,11]. In addition, it is difficult to evaluate the physiological functions of storage and voiding of the bladder while it is being filled with saline or iodinated contrast at a supraphysiologic rate. As such, UDS have not been widely utilized as an early test to study the progression of bladder function and its changes over the time in the OAB population. That said, it is likely that there are incredibly important phenotypic differences in the manifestation of bladder dysfunction leading to OAB, and that early detection through objective measures such as non-invasive (NI) multi-channel UDS could assist in categorizing patients into the appropriate therapeutic intervention.

The benefits of a non-invasive and ambulatory method to monitor the bladder and detrusor activity are multifold. First, a non-invasive system would greatly reduce patient discomfort and anxiety while performing the study. Ideally, it would also eliminate the artifactual results and have

higher specificity/resolution than conventional UDS in identifying bladder changes. An ambulatory device would make available a method for both inpatient and outpatient evaluation as well as make it more feasible for patients to undergo regular assessment. This would eliminate the need for a time- and resource-consuming study such as conventional multi-channel UDS. With consideration of the expectations, non-invasive bladder EMG with decreased electro-mechanical artifact has been introduced by several groups [12,13,14,15]. However, it has not found a significant enough foothold in the clinic to meaningfully and positively impact patient care. An example of such a sensitive, non-invasive EGG-monitoring system has been successfully developed for applications in the gastro-intestinal tract. These authors were able to accurately assess slow-wave propagation of the stomach [16,17,18]. With such obvious need for noninvasive bladder monitoring, we adapted this technology to develop a high-resolution and non-invasive multi-channel urodynamic system (NI multi-channel UDS) combined with novel spatial waveform analysis to determine a signature electrical signal pattern from the urinary bladder in healthy volunteers and provide actionable information that is clinically practical for diagnosis and prognosis.

Results

The NI multi-channel UDS system utilizes the full benefit of high technology for data transfer from Cyton, a data collecting device, to the OpenBCI USD Dongle and OpenBCI_GUI software using Bluetooth technology real-time (**Figure 4.1**). We validated the feasibility of our study design having electrodes configuration and a data collection system for use in comparison to uroflow, one of the conventional diagnostic tools to determine dysfunctional voiding behavior of human subjects. The uroflow data of 14 human subjects (N=6 male and N=8 female), including

basic information and information, and its relevant information are tabulated in **Table 4.1**. These uroflow data confirms that all human subjects participated in this study have healthy voiding behavior. In parallel, we confirmed that electrical signaling from surface electrodes was successfully transferred utilizing our NI multi-channel UDS system and we were able to perform data analysis from collected data. Given that we performed a synchronous utilization of an uroflow and our NI multi-channel UDS system, our study design suggests that the NI multi-channel UDS system does not interrupt a process of diagnosis utilizing conventional tools in the Urology clinic.

Our NI multi-channel UDS system includes a customized array of electrodes specifically designed for collecting electrical signals from the urinary bladder (**Figure 4.2**). To prepare a customized array of electrodes, cleanroom fabrication was performed using standard CMOS processes as shown in the Experimental Section/Methods. The finished post cleanroom-produced Silicon wafer is shown in **Figure 4.2**c with gold on the top layer waiting to be screen printed with the Ag/AgCl ink. Subsequently, the wafer was screen printed with 75 um thick stainless steel stencil and it yielded a finished Ag/AgCl layer of 37.5 um. The device was then transfer-printed to a bilayer silicone substrate (Ecoflex/Silbione) using water soluble tape as shown in **Figure 4.2**d. The self-adhering device was then placed to the subject and subsequently the PET backing was ready to be removed before the data collection began (**Figure 4.2**e). Then, we confirmed that our customized array of electrodes was securely attached to the skin of the lower abdomen of each human subject during and in between the time course of pre-, voluntary- and post-voiding phase.

After we fully validated our system, electrical signals from the urinary bladder of N= 14 subject were collected. Electrical signals from all electrodes were successfully transferred to OPENBCI_GUI software, recorded in the designated folder of the laptop and then plotted to visualize voltage changes in the bladder. Then, we wrote code in Python using Jupiter software to

eliminate the signals at 60 Hz as a process of noise filtering. Examples of basic time series plots from each electrode from one male and female subject are shown in **Figure 4.3**b **and 4.4**b. Time (minute, min) is shown on the x-axis and voltage (mV) is denoted on the y-axis. After the noise filtering process, both periods and amplitude of electrical signals from the urinary bladder detected from all eight electrodes were more consistent as compared to those without noise filtering process **(Figure 4.3**b **and 4.4**b**)**. Pattern of electrical signals from each electrode was not identical with and without noise filtering process. Further, the processed time series after the noise filtering process is shown in **Figure 4.3**a for a male subject and **Figure 4.4**a for a female subject. The three boxes correspond to the signal from the pre-voiding (5 minutes 30 sec), voiding (various duration), and post-voiding (5 minutes). Although the duration of voiding differs from subject to subject, our results show strong EMG signatures from subjects (male and female) during the period of voiding (**Figure 4.3**c and 4.**4**c). Lastly, the spatial locations of each electrode as well as the processed signals from each subject is depicted on **Figure 4.3**c for a male subject and **Figure 4.4**c for a female subject. Subject-specific phenotype of electrical signal shown in the time series plot suggests that our NI multi-channel UDS system is stable to sense inter-subject variability but also determine a common feature of electrical signal from the urinary bladder.

Discussion

In distinction of ureteral or GI musculature, the bladder architecture contains randomly arranged fascicles of smooth muscle. Myofibroblasts, or interstitial cells, exist within the lamina propria and detrusor layers, and have been proposed to have a pace-making role in spontaneous activity of the bladder. These cells have been shown to be spontaneously active in the “normal” bladder, and exaggerated spontaneous contractions could contribute to the development of detrusor

overactivity. The class model of OAB is that of urodynamically demonstrated detrusor overactivity, although this finding may not be apparent in a majority of patients with OAB symptoms suggesting the need for development and advancement of the OAB monitoring system. Kinder, *et al* demonstrated that non-invasive bladder EMG can successfully detect slow voltage change in bipolar electrode signals during the voiding phase, and can distinguish their signals from bipolar electrode signals caused by abdominal and other striated muscle activity. However, the previous group did not make note of issues regarding movement artifacts. In this study, we successfully eliminated movement artifacts using Jupiter software and Python program language for noise filtering of signals at 60 Hz and sorted out the desired urodynamic parameters from original data. Artifact removal signal processing methods utilized in our study were adapted from previous study, which aimed to extract gastric signal utilizing EEG [17,18] with a multi-channel electrode system.

Given that several factors including age and hormonal change may affect urodynamic parameters at the time of NI multi-channel UDS recording, it is striking that our system revealed a signature pattern of electrical signals from urinary bladder over the course of pre-, voluntary and post- voiding, which was consistent in 14 subjects. The use of a custom electrode array that leveraged flexible electronics technology enabled conformal contact to the lower abdomen during the entire duration of the recording. Ag/AgCl was chosen to be the material for the sensor layer due to high signal-to-noise ratio, lower skin-to-electrode impedance, and the non-polarizable nature of Ag/AgCl electrodes which allows Cl^- ion to take part in free charge exchange which prevents charge buildup [18,19,20]. It was also previously demonstrated that this class of Ag/AgCl flexible electrodes were successful in measuring other biopotential signals, i.e: EGG, therefore it was appropriate to choose such materials to be the basis of our EMG electrodes due to its superior recording quality compared to gold electrodes [18,19,20]. Further, the combination of ambulatory

monitoring via openBCI biopotential board and the use of uroflow allows a more holistic assessment of a subject's bladder activity.

After a new medical device is fully developed and available for its distribution, its successful implementation to clinical practice is dependent on a health professional's decision. One of the major determinants of the health professional's decision is known to be technical aspects of the new device which include durability, extent of improvement, handling, invasiveness, overall assessment and product generation [21]. Our NI multi-channel UDS system is expected to meet all these technical aspects. First of all, the durability of our NI multi-channel techniques has already been validated for gastric motility disorders [16,17]. Second, NI multi-channel UDS Code set using Jupyter software and Python program language determined in this study can be modified for other urological complications in a symptom-specific manner suggesting unlimited extent of improvement. Third, management and maintenance of our NI multi-channel UDS are straightforward. There is almost no limit for merging the NI multi-channel UDS system to other clinical procedures, including conventional UDS, sacral neuromodulation, uroflow study, needle biopsy and many others. Therefore, adaptation of NI multi-channel UDS does not require a dynamic adaptation for clinicians and staff to suddenly stop performing conventional UDS or operate other clinical applications less frequently. Fourth, our NI multi-channel UDS will reduce the need for invasive testing and improve our diagnostic capabilities in the early stages of symptom development and will also promote the development of more targeted strategies, as opposed to the current algorithmic approach through first, second, and third-line therapies. Fifth, product generation and distribution of our system are highly feasible. Cyton, a compact hexagon board, is a cost efficient, user-friendly and light-weight device. Taken together, this implies unlimited

potential for the NI multi-channel UDS system to be successfully implemented in the clinic as a diagnostic, monitoring, and therapeutic treatment evaluation system.

Given that our current study provides a foundation for further studies to determine a signature pattern in electrical signal from health bladder vs dysfunctional bladder, physiological pattern of dysfunctional bladder can be further sub-categorized into each urological symptom, which includes but not limited to OAB, chronic pelvic pain syndrome (CPPS), lower urinary tract symptoms (LUTS) and benign prostatic hyperplasia (BPH). Furthermore, prognostic urodynamic parameters of successfully OAB sacral neuromodulation can be established utilizing our NI multi-channel UDS, which are expected to suggest better OAB treatment prognosis as well as a practical advice for OAB patients to choose their therapeutic options. Therefore, NI multi-channel UDS has a great potential to be a three-in-one, multi-purpose, clinically-practical system for diagnosis of dysfunctional bladder, repetitive monitoring, and evaluation of treatment. This feature is expected to provide enormous benefits for both clinicians and patients by suggesting a consistent data set over the course of OAB symptoms.

Experimental Section/Methods

NI Multi-Channel UDS System Preparation:

Our NI multi-channel UDS consisted of a customized array of electrodes, two 3M RedDot Sensor, ECG/EMG snap electrode cables, a customized breakout board, a Cyton board, an OpenBCI USB Dongle, OPENBCI_GUI software, and a laptop (Figure 1). In detail, ECG/EMG snap electrode cables are connected to the electrode pins located in the Cyton board as ground and reference. Meanwhile, the flexible sensor array was also connected to the Cyton board via a

customized breakout board. OpenBCI USB Dongle is connected to the laptop and the OPENBCI_GUI software is turned on upon data collection.

Electrodes Array Fabrication:

A silicon wafer was pre-cleaned with acetone, IPA, DI water, IPA followed by drying with N_2 gun. The wafer was then baked on a 180°C hotplate to dry. Polydimethysiloxane (PDMS) was spun coated on the clean wafer at 4000 rpm which would act as a weakly adhering substrate for subsequent fabrication steps. The wafer was then spun coated with Polyimide (HD Microsystems, Inc. - Parlin, NJ) at 4000 rpm followed by a soft bake at 110°C for 1 min and at 150°C for 5 min. It was then followed by a full hard bake in a N_2 rich environment oven at 300°C. Metallization of 10 nm chrome and 250 nm gold was then followed (Temescal BJD 1800 E-Beam Evaporator - Livermore, CA). Sensors (8.6 mm diameter) and interconnects (200 um width) were defined via standard microfabrication procedures (photolithography, development, and metal wet etching). Another layer of polyimide was then applied using the same parameters as above. Photolithography and reactive ion etching (RIE) with O_2 plasma was then followed to define the bottom and top polyimide layer which acted as insulator layers. Silver/silver chloride ink (Creative Materials, Inc. - Ayer, MA) was then screen printed onto the sensor areas with a stainless steel stencil (Metal Etch Services, Inc. - San Marcos, CA). A custom zero insertion force (ZIF) connector was then interfaced with the electrode array using anisotropic tape which facilitated bonding (3M, Inc. - Saint Paul, MN) by applying heat and pressure on the bonding sites. Water soluble tape (3M, Inc. - Saint Paul, MN) was then used to transfer print the device from the silicon wafer to a flexible silicone substrate made on a 5" petri dish that was spun coated at 3000 rpm with Ecoflex (Smooth On, Inc. - Macungie, PA) which acted as a backbone silicone and Silbione RT Gel (Elkem, Inc. - Brunswick, NJ) which acted as an adhesive silicone. The silicone substrate and

the device were then peeled off and transferred to a thin sheet of PET (Grafix - Maple Heights, OH) which acted as a backing that eased handling of the device.

NI multi-channel UDS recordings:

All procedures in this study were performed after approval (HRPP #180602) by the Institutional Review Board (IRB) and University of California San Diego (UCSD) Human Research Protections Program (HRPP). Subjects were recruited at University of California San Diego (UCSD) Health System and in the Urology Clinic at the VA Hospital San Diego. Each subject has the electrodes placed after reporting the sensation of a full bladder. Before the device application, the lower abdomen and suprapubic region was prepped using alcohol pads and a skin prep gel to exfoliate dead skin. The lower abdomen and suprapubic region is prepped using alcohol pads and a skin prep gel. A ground electrode was placed on the lower left flank, and an additional reference electrode was placed near the flexible sensor array. For both ground and reference signals, 3M RedDot surface electrodes were used.

Silbione allowed the device to conformally attach to the suprapubic area. The ZIF connector was attached to an adapter board (Adafruit Industries, Inc - New York, NY) which was connected to a Bluetooth biopotential board (OpenBCI, Inc) alongside ground and reference electrodes (3M Red Dot, 3M, Inc - Saint Paul, MN). The device was applied about 5 mm above the pubic symphysis, followed by the peeling of the PET backing. The the ZIF connector was then attached to an adapter board (Adafruit Industries, Inc - New York, NY) which was connected to a biopotential board (OpenBCI, Inc) via jumper cables along with ground and reference electrodes (3M Red Dot, 3M, Inc - Saint Paul, MN).

Recordings were performed on 14 healthy subjects (N = 8 females and N = 6 males, average age: 32 years, age range 20-44 years) over the course of pre-voiding phase (storage/filling phase, 5 minutes 30 seconds), voluntary voiding phase (the entire duration to empty the bladder), and post-voiding phase (5 minutes). Please note that the duration of voiding differed for each participant.

Data Collection:

Data recording was streamed wireless via the openBCI GUI installed on a Macbook Pro (Apple, Inc. - Cupertino, CA). OpenBCI was chosen based on the previously published findings that indicated enough artifact and noise rejection for an ambulatory EGG monitoring using the same biopotential system.

Data Processing:

To process the noisy 8 channel EMG signal, a 30 Hz - 122 Hz bandpass butterworth filter was applied to the data set. Next, a 60 Hz bandstop butterworth filter to account for the powerline frequency was applied. These two filters were both created to an arbitrary order of 5. Lastly, the artifacts of the filtered signal were removed using a Wiener artifact rejection filter with a window size of 6 and no window noise. To plot all of the channels distinctly, their means were centered and then spread every 2 volts to split the channels into 8 individual waveforms. They were all plotted against their respective times ordered by each patient separated by both gender and 'pre-voiding', 'voiding', and 'post-voiding' signals.

Acknowledgments

The authors would like to acknowledge graphic design assistance from Sebastian Podiono. J.F.K, S.L, and H.L contributed equally to this work. This work was performed in part at the San Diego Nanotechnology Infrastructure (SDNI) of UCSD, a member of the National Nanotechnology Coordinated Infrastructure (NNCI), which is supported by the NSF grant ECCS-1542148.

This chapter, in full, is currently being prepared for submission for publication of this material. Jonas F. Kurniawan, Sanghee Lee, Hoang-Kim Le, Andrew K. L. Nguyen, Nathan L.J. Sit, Timothy Pham, Boris Tjhia, Ryan Gottlieb, Carleen Li, Andrew J. Shin, Hassler Bueno Garcia, Vincent M. Wu, Tris R Mendoza, Thomas DiPina, George Chiang, Gladys Ornelas, Christina A.M. Jamieson, Yahir Santiago-Lastra, Todd P. Coleman. The dissertation author was the primary investigator of this material.

References

[1] Weld, K. J., & Dmochowski, R. R. (2000). Association of level of injury and bladder behavior in patients with post-traumatic spinal cord injury. *Urology*, *55*(4), 490-494.

[2] Dallosso, H. M., Matthews, R. J., McGrother, C. W., Donaldson, M. M., Shaw, C., & Leicestershire MRC Incontinence Study Group. (2004). The association of diet and other lifestyle factors with the onset of overactive bladder: a longitudinal study in men. *Public health nutrition*, *7*(7), 885-891.

[3] Dallosso, H. M., McGrother, C. W., Matthews, R. J., & Donaldson, M. M. (2004). Nutrient composition of the diet and the development of overactive bladder: a longitudinal study in women. *Neurourology and urodynamics*, *23*(3), 204-210.

[4] Mitsui, T., Kira, S., Ihara, T., Sawada, N., Nakagomi, H., Miyamoto, T., ... & Takeda, M. (2020). Metabolism of fatty acids and bile acids in plasma is associated with overactive bladder in males: potential biomarkers and targets for novel treatments in a metabolomics analysis. *International urology and nephrology*, *52*(2), 233-238.

[5] Lau, H. H., Su, T. H., & Huang, W. C. (2021). Effect of aging on lower urinary tract symptoms and urodynamic parameters in women. *Taiwanese Journal of Obstetrics and Gynecology*, *60*(3), 513-516.

[6] Lightner, D. J., Gomelsky, A., Souter, L., & Vasavada, S. P. (2019). Diagnosis and treatment of overactive bladder (non-neurogenic) in adults: AUA/SUFU guideline amendment 2019. *The Journal of urology*, *202*(3), 558-563.

[7] Reynolds, W. S., Fowke, J., & Dmochowski, R. (2016). The burden of overactive bladder on US public health. *Current bladder dysfunction reports*, *11*(1), 8-13.

[8] Milosevic, S., Joseph-Williams, N., Pell, B., Cain, E., Hackett, R., Murdoch, F., ... & Harding, C. (2021). Conducting invasive urodynamics in primary care: qualitative interview study examining experiences of patients and healthcare professionals. *Diagnostic and Prognostic Research*, *5*(1), 1-9.

[9] Shaw, C., Williams, K., Assassa, P. R., & Jackson, C. (2000). Patient satisfaction with urodynamics: a qualitative study. *Journal of advanced nursing*, *32*(6), 1356-1363.

[10] Drake, M. J., Doumouchtsis, S. K., Hashim, H., & Gammie, A. (2018). Fundamentals of urodynamic practice, based on International Continence Society good urodynamic practices recommendations. *Neurourology and urodynamics*, *37*(S6), S50-S60.

[11] Suskind, A. M., Clemens, J. Q., Kaufman, S. R., Stoffel, J. T., Oldendorf, A., Malaeb, B. S., ... & Cameron, A. P. (2015). Patient perceptions of physical and emotional discomfort related to urodynamic testing: a questionnaire-based study in men and women with and without neurologic conditions. *Urology*, *85*(3), 547-551.

[12] Kinder, M. V., Van Waalwijk van Doorn, E. S. C., Gommer, E. D., & Janknegt, R. A. (1998). A non-invasive method for bladder electromyography in humans. *Archives of physiology and biochemistry*, *106*(1), 2-11.

[13] Combs, A. J., Grafstein, N., Horowitz, M., & Glassberg, K. I. (2005). Primary bladder neck dysfunction in children and adolescents I: pelvic floor electromyography lag time—a new noninvasive method to screen for and monitor therapeutic response. *The Journal of urology*, *173*(1), 207-211.

[14] Van Batavia, J. P., Combs, A. J., Hyun, G., Bayer, A., Medina-Kreppein, D., Schlussel, R. N., & Glassberg, K. I. (2011). Simplifying the diagnosis of 4 common voiding conditions using uroflow/electromyography, electromyography lag time and voiding history. *The Journal of urology*, *186*(4S), 1721-1727.

[15] Combs, A. J., Van Batavia, J. P., Horowitz, M., & Glassberg, K. I. (2013). Short pelvic floor electromyographic lag time: a novel noninvasive approach to document detrusor overactivity in children with lower urinary tract symptoms. *The Journal of urology*, *189*(6), 2282-2286.

[16] Gharibans, A. A., Kim, S., Kunkel, D. C., & Coleman, T. P. (2016). High-resolution electrogastrogram: a novel, noninvasive method for determining gastric slow-wave direction and speed. *IEEE Transactions on Biomedical Engineering*, *64*(4), 807-815.

[17] Gharibans, A. A., Smarr, B. L., Kunkel, D. C., Kriegsfeld, L. J., Mousa, H. M., & Coleman, T. P. (2018). Artifact rejection methodology enables continuous, noninvasive measurement of gastric myoelectric activity in ambulatory subjects. *Scientific reports*, *8*(1), 1-12.

[18] Kurniawan, J. F., Tjhia, B., Wu, V. M., Shin, A., Sit, N. L., Pham, T., ... & Coleman, T. P. (2021). An Adhesive-Integrated Stretchable Silver-Silver Chloride Electrode Array for Unobtrusive Monitoring of Gastric Neuromuscular Activity. *Advanced Materials Technologies*, *6*(5), 2001229.

[19] Tallgren, P., Vanhatalo, S., Kaila, K., & Voipio, J. (2005). Evaluation of commercially available electrodes and gels for recording of slow EEG potentials. *Clinical Neurophysiology*, *116*(4), 799-806.

[20] Albulbul, A. (2016). Evaluating major electrode types for idle biological signal measurements for modern medical technology. *Bioengineering*, *3*(3), 20.

[21] Felgner, S., Ex, P., & Henschke, C. (2018). Physicians' decision making on adoption of new technologies and role of coverage with evidence development: a qualitative study. *Value in Health*, *21*(9), 1069-1076.

Figures

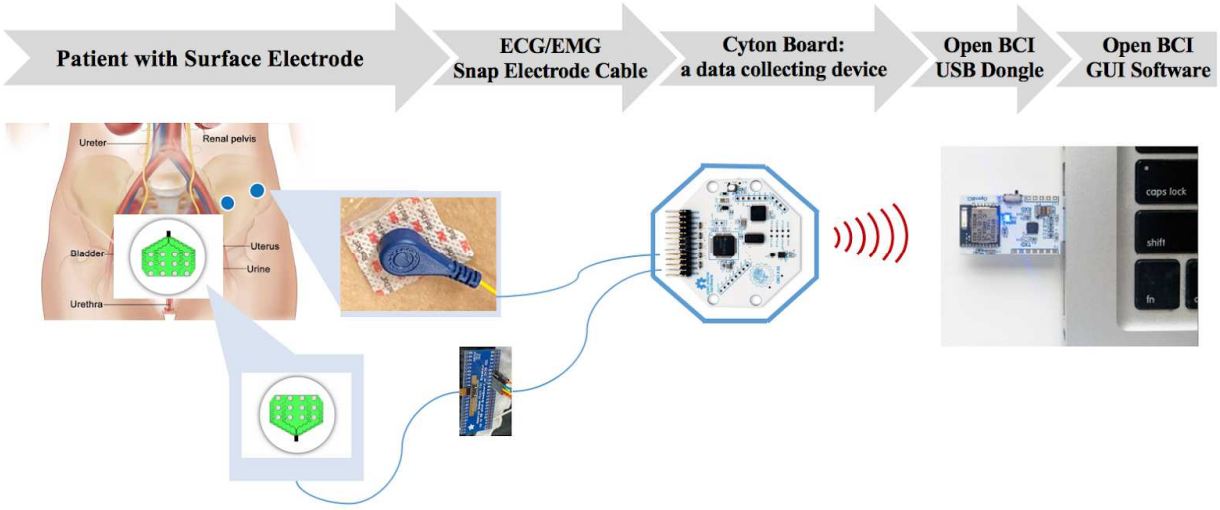

Figure 4.1. Illustration of a NI multi-channel UDS system to record urinary bladder electrical activity during pre-, voluntary-, and post-voiding phase utilizing a multichannel array, 3M RedDot sensors, a Cyton board, OpenBCI USB dongle, and OpenBCI Software.

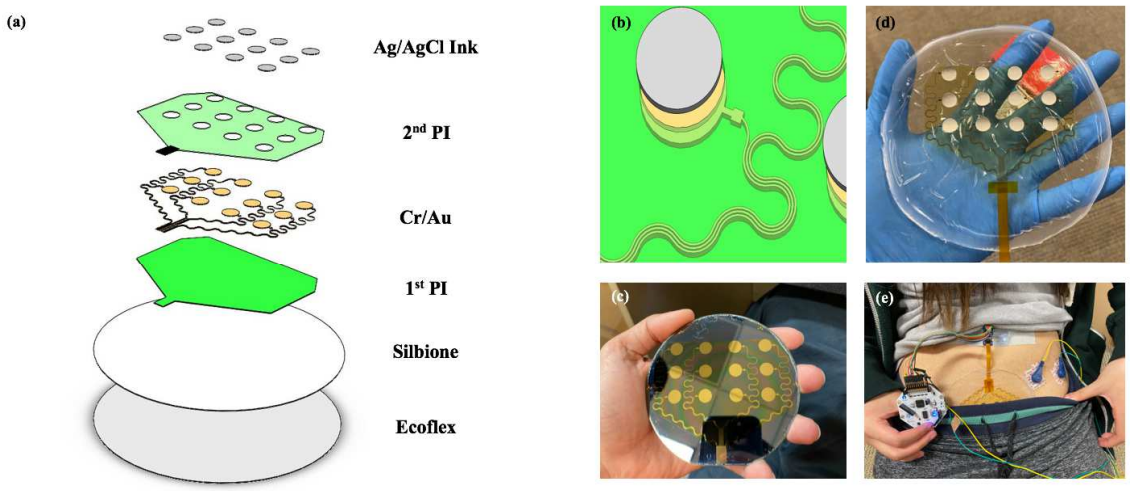

Figure 4.2. (a) Exploded view of the entire device (8.6 mm sensor diameter and 200 um interconnect width). **(b)** Cross section view of one of the sensors, consisting of the bottom PI layer, Au, the top PI layer, and Ag/AgCl printed layer. **(c)** Post cleanroom EMG device fabricated on a silicon wafer with Au on top layer before the screen printing process of Ag/AgCl has begun. **(d)** Screen printed EMG device (Ag/AgCl ink - 37.5 um thickness) that was transferred into a self-adhering flexible silicone substrate. (**e)** EMG device placed on a subject; alongside the rest of the experimental setup (Cyton board, breakout board, and RedDot electrodes).

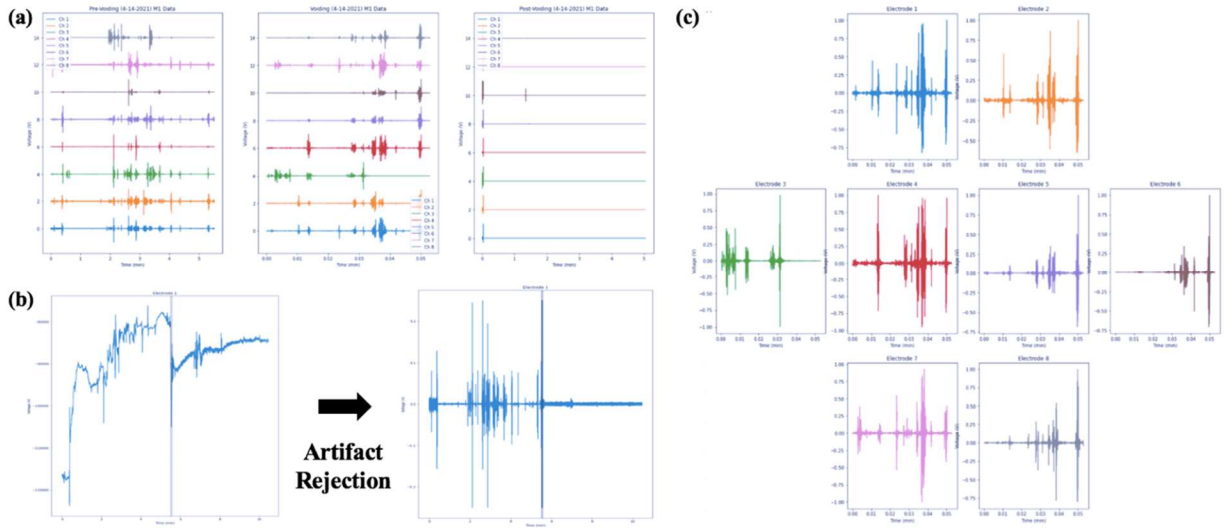

Figure 4.3. (a) Time series plot of a male subject after applying artifact rejection filter. The boxes from left to right represent pre-voiding, voiding, and post voiding signals. The data shown are for 8 different electrode channels **(b)** A representative time series plot shown during a voiding period, the graph on the left shows the raw signal, meanwhile the graph on the right shows the processed signal by applying the artifact rejection filter. **(c)** The spatial arrangement of the electrodes on the subject. Each box represents a signal from a single electrode, the top row represents channel 1 and 2, followed by channel 3, 4, 5, 6 in the middle, and finally channel 7 and 8 at the bottom.

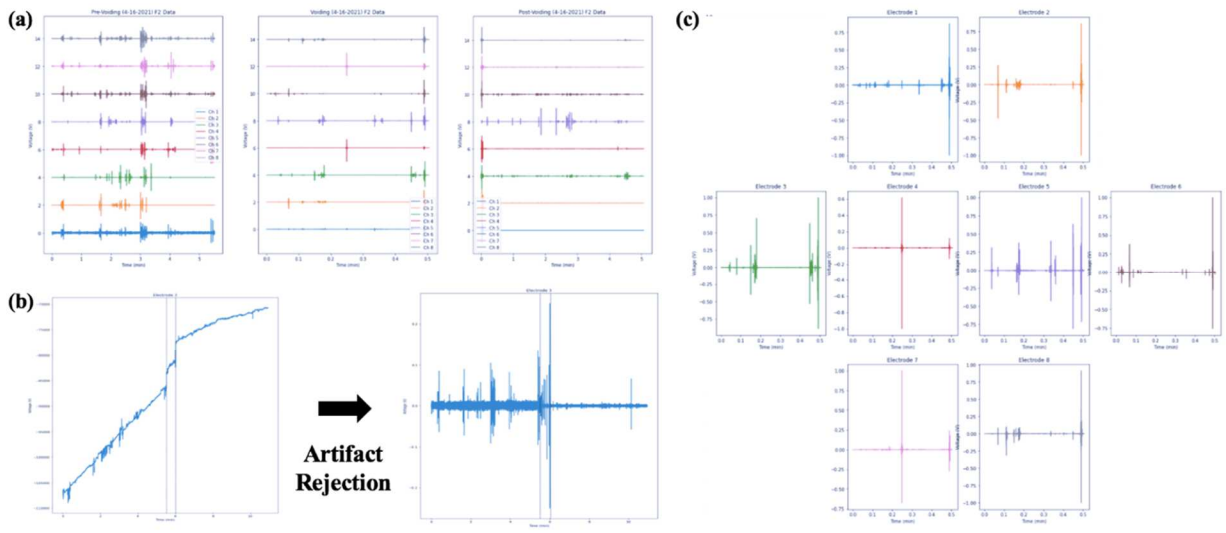

Figure 4.4. (a) Time series plot of a female subject after applying artifact rejection filter. The boxes from left to right represent pre-voiding, voiding, and post voiding signals. The data shown are for 8 different electrode channels **(b)** A representative time series plot shown during a voiding period, the graph on the left shows the raw signal, meanwhile the graph on the right shows the processed signal by applying the artifact rejection filter. **(c)** The spatial arrangement of the electrodes on the subject. Each box represents a signal from a single electrode, the top row represents channel 1 and 2, followed by channel 3, 4, 5, 6 in the middle, and finally channel 7 and 8 at the bottom.

Tables

Table 4.1. Statistics of various subjects which included basic information such as gender, location of experiment, and age. Voiding information was extracted from the uroflow data which were collected during the voiding period of each subject.

Date of Data Collection	Gender	Location of Data Collection	Age	Voiding Volume (ml)	Voiding Duration (s)	Urine Flow Rate (ml/s)
3/30/21	F1	KOP	35	262	11	23.82
3/30/21	F2	KOP	39	416	58	7.17
3/30/21	F3	KOP	39	293	13	22.54
3/30/21	M1	KOP	22	300	43	6.98
4/1/21	F1	Hillcrest	31	245	21.4	11.45
4/1/21	F2	Hillcrest	33	188	11.2	16.79
4/9/21	F1	KOP	20	154	12	12.83
4/9/21	M1	KOP	28	196	23	8.52
4/14/21	M1	VA	30	620	42.9	14.45
4/14/21	M2	VA	34	100	87	1.15
4/14/21	M3	VA	31	400	19	21.05
4/16/21	F1	VA	28	700	57	12.28
4/16/21	F2	VA	32	525	30	17.50
4/16/21	M1	VA	44	300	20	15.00